Check for updates

OCEANOGRAPHY

C:H:N:O:P stoichiometry and oxygen demand of marine organic matter are driven by phytoplankton ecophysiology

Shlomit Sharoni[1]*, Keisuke Inomura[2], Stephanie Dutkiewicz[1,3], Oliver Jahn[1], Gregory L. Britten[4], Michael J. Follows[1]

Copyright © 2026 The Authors, some rights reserved; exclusive licensee American Association for the Advancement of Science. No claim to original U.S. Government Works. Distributed under a Creative Commons Attribution NonCommercial License 4.0 (CC BY-NC).

Although the hydrogen and oxygen content of marine phytoplankton plays a critical role in determining oceanic O_2 consumption rates, shaping habitat for anaerobic metabolism, they are often assumed to be constant in biogeochemical studies, resulting in biased estimates of respiration rates. Here, by simulating phytoplankton allocation in a general circulation model, we predict latitudinal variations in phytoplankton C:H:N:O:P composition and corresponding O_2 demand. These patterns are driven by physiological adaptation to environmental conditions and are consistent with observations. Subtropical phytoplankton have more C—O bonds and lower O_2 demand, as they contain more carbohydrates than higher-latitude populations. We test the sensitivity of O_2 inventory and regenerated C via the biological pump (C^{soft}) to plausible bounds of cellular allocation and find that the global O_2 inventory and C^{soft} decrease by ~11 and 14%, respectively, when a cell shifts from carbohydrate-rich to protein-rich biomass. Our findings demonstrate that biochemical remodeling of phytoplankton composition mediates large-scale patterns and oceanic budgets of O_2 and C.

INTRODUCTION

The ratios by which marine phytoplankton acquire inorganic elements and incorporate them into their cellular material (i.e., their elemental composition) couple the global cycles of carbon (C), nitrogen (N), phosphorus (P), trace elements, and oxygen (O), and, therefore, play a fundamental role in shaping biogeochemical cycles. The relative ratio of N:P in seawater and phytoplankton indicates whether cells are nitrate or phosphate limited and regulates nitrogen fixation and denitrification rates (*1*–*7*). The ratio of C to the limiting nutrient dictates the amount of atmospheric carbon dioxide (CO_2) that can be sequestered in the deep ocean via the "biological pump" (*8*–*10*). The hydrogen (H) and O content of the organic matter further provides an estimate of dissolved oxygen (O_2) consumption and nitrate loss (denitrification) during aerobic and anaerobic respiration of organic matter (*11*–*13*). Because organic matter respiration is the main route by which dissolved O_2 is lost from the ocean interior (*14*, *15*), understanding and quantitatively modeling the composition of planktonic cells and the factors controlling it is crucial for understanding the O_2 budget in the ocean.

Two main metrics are often used to quantify O_2 loss during organic matter respiration (for more information, see Eqs. 5 and 6 and their corresponding text). The first is the total respiration quotient ($R_{-\Sigma O2:C}$; mol O_2/mol C), which reflects the molar ratio of O_2 consumed per CO_2 released during complete aerobic respiration of organic matter. The second is oxygen demand ($R_{-\Sigma O2:P}$; mol O_2/mol P), which expresses the amount of O_2 consumed per unit P released during complete aerobic respiration of organic matter, and reflects variability both in $R_{-\Sigma O2:C}$ and the C:P of organic matter (C:P): $R_{-\Sigma O2:P} = R_{-\Sigma O2:C} \times$ (C:P). Both $R_{-\Sigma O2:C}$ and $R_{-\Sigma O2:P}$ are used in Earth system models to estimate O_2 consumption from export production, depending on whether organic matter is expressed in terms of C or P, respectively.

Traditionally, the stoichiometric equation representing the production and complete aerobic heterotrophic respiration of a phytoplankton cell (estimated from measured C:N:P of 106:16:1 in marine phytoplankton) is the Redfield-Ketchum-Richards (RKR) equation (*16*)

$$106CO_2 + 16HNO_3 + H_3PO_4 + 122H_2O \leftrightarrow (CH_2O)_{106}(NH_3)_{16}(H_3PO_4) + 138O_2 \quad (1)$$

where production is the forward reaction and respiration is the reverse. Here, it is assumed that organic matter is composed mainly of carbohydrates (CH_2O), ammonia (NH_3), and phosphate (H_3PO_4). This assumption resulted in a "bulk" theoretical elemental composition of $C_{106}H_{263}O_{110}N_{16}P$, $R_{-\Sigma O2:C}$ of 1.3 (mol O_2/mol C), and $R_{-\Sigma O2:P}$ of 138 (mol O_2/mol P). Here, the $R_{-\Sigma O2:P}$ value of 138 accounts for 106 mol O_2 per mol P consumed during carbohydrate oxidation (assuming $R_{-\Sigma O2:C} = 1.0$ for carbohydrate; Fig. 1B), and 32 mol O_2 per mol P consumed during nitrification (see Box 1). However, phytoplankton are not made of only carbohydrates but, rather, are protein-synthesizing microorganisms, with protein accounting for 40 to 60% of phytoplankton cell carbon (*17*). Lipids and carbohydrates contribute 10 to 40% of cell carbon (Fig. 1A). Carbohydrates are a relatively oxidized form of organic matter, whereas proteins and lipids are more reduced (proteins contain reduced nitrogen, and both proteins and lipids contain CH_2 chains). Therefore, the downstream biosynthesis of proteins and lipids from initially fixed carbohydrates releases O_2, increasing the cell's overall $R_{-\Sigma O2:P}$ and $R_{-\Sigma O2:C}$ (Fig. 1B).

The total respiration quotient ($R_{-\Sigma O2:C}$) and oxygen demand ($R_{-\Sigma O2:P}$) of organic matter can be estimated using different approaches. Using the average biochemical composition of the dominant macromolecules and their relative abundances in marine phytoplankton cells, Laws and Anderson have (theoretically) estimated an average $R_{-\Sigma O2:P}$ of 150 mol O_2/mol P and $R_{-\Sigma O2:C}$ of 1.40 mol O_2/mol C

[1]Department of Earth, Atmospheric and Planetary Sciences, Massachusetts Institute of Technology, Cambridge, MA, USA. [2]Graduate School of Oceanography, University of Rhode Island, Narragansett, RI, USA. [3]Center for Sustainability Science and Strategy, Massachusetts Institute of Technology, Cambridge, MA, USA. [4]Biology Department, Woods Hole Oceanographic Institution, Woods Hole, MA, USA.
*Corresponding author. Email: shlomit.sharoni@mail.huji.ac.il

Downloaded from https://www.science.org at University of Rhode Island on November 06, 2026

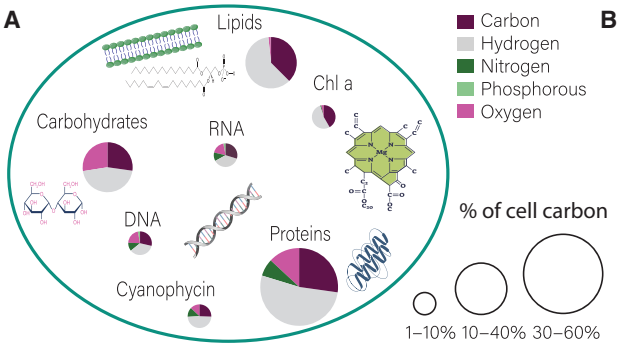

B

Macromolecule	Average formula	$-\sum O_2$:C
Proteins	$C_{5.3}H_{10.1}N_{1.4}O_{2.5}S_{0.07}$	1.59
DNA	$C_{9.50}H_{11.75}N_{3.75}O_{7.00}P$	1.57
RNA	$C_{9.75}H_{12.25}N_{3.75}O_{6.00}P$	1.62
Carbohydrates	$C_6H_{10}O_5$	1.00
Lipids	$C_{37}H_{60}O_{4.5}S_{0.09}$	1.36
Phospholipids	$C_{43}H_{76}N_{0.7}O_{8.7}P$	1.39
Chlorophyll a	$C_{55}H_{72}N_4O_5Mg$	1.37
Polyphosphate	H_3PO_4	NA
Cyanophycin	$C_{10}H_{19}N_5O_5$	1.85

Fig. 1. A schematic representation of the macromolecular composition of a phytoplankton cell. (**A**) Average composition of a phytoplankton cell. The size of the pie charts represents the estimated contribution of each macromolecular pool to cell carbon (%), whereas the proportions within the pie charts indicate the relative molar content of elements in each type of macromolecule. This scheme is inspired by Liefer *et al.* (*62*). (**B**) Average formula and total respiration quotient ($R_{-\Sigma O2:C}$, mol O_2/mol C) of major macromolecules identified in marine phytoplankton. The average formula and total respiration quotient of proteins, lipids, and nucleic acids are based on major amino acids identified in marine phytoplankton (*69*–*72*), lipids identified in marine phytoplankton (*68*, *80*), and an assumed equimolar distribution of the four deoxyribonucleotides and ribonucleotide bases, respectively (tables S2 and S3).

Box 1. Stoichiometric equations for organic matter respiration.

Aerobic heterotrophic respiration of organic matter to ammonia and carbon dioxide can be represented by the following equation (*12*)

$$C_aH_bO_cN_dP + \left(a + \frac{1}{4}b - \frac{1}{2}c - \frac{3}{4}d + \frac{5}{4}\right)O_2 \rightarrow aCO_2 + dNH_3 + H_3PO_4 + \left(\frac{1}{2}b - \frac{3}{2}d - \frac{3}{2}\right)H_2O \quad (2)$$

The amount of oxygen consumed during this reaction, i.e., the "partial" respiration quotient ($R_{-O2:C}$; mol O_2/mol C) can be estimated from the bulk C:H:N:O:P stoichiometry (Materials and Methods)

$$R_{-O2:C} = \frac{a + \frac{1}{4}b - \frac{1}{2}c - \frac{3}{4}d + \frac{5}{4}}{a} \quad (3)$$

Nitrification of ammonia to nitrate requires two additional O_2 for each NH_3, yielding the following relationship, which represents complete aerobic heterotrophic respiration of organic matter to nitrate (Materials and Methods)

$$C_aH_bO_cN_dP + \left(a + \frac{1}{4}b - \frac{1}{2}c + \frac{5}{4}d + \frac{5}{4}\right)O_2 \rightarrow aCO_2 + dNO_3 + H_3PO_4 + \left(\frac{1}{2}b - \frac{3}{2}d - \frac{3}{2}\right)H_2O \quad (4)$$

Here, the total oxygen demand ($R_{-\Sigma O2:P}$; mol O_2/mol P) and the total respiration quotient ($R_{-\Sigma O2:C}$; mol O_2/mol C) representing complete oxidation (including nitrification) are

$$R_{-\Sigma O2:P} = a + \frac{1}{4}b - \frac{1}{2}c + \frac{5}{4}d + \frac{5}{4} \quad (5)$$

$$R_{-\Sigma O2:C} = \frac{a + \frac{1}{4}b - \frac{1}{2}c + \frac{5}{4}d + \frac{5}{4}}{a} \quad (6)$$

The total respiration quotient ($R_{-\Sigma O2:C}$) is larger than the partial respiration quotient ($R_{-O2:C}$) that does not account for the O_2 consumed during nitrification. For example, the Redfield-Ketchum-Richards (RKR) equation indicates that $R_{-\Sigma O2:C} = 1.3$, whereas $R_{-O2:C} = 1.0$.

(*18*, *19*). This "bottom-up approach" relies on culture-based laboratory estimates of phytoplankton composition and assumes a fixed average stoichiometry, without accounting for natural variability in species and environmental conditions. In contrast, "top-down approaches" estimate $R_{-\Sigma O2:P}$ and $R_{-\Sigma O2:C}$ indirectly, by measuring the ratio of dissolved, inorganic nutrients in the ocean. For example, $R_{-\Sigma O2:P}$ can be estimated by measuring the deviation of phosphate and O_2 from their "preformed" values (where preformed is defined as the concentration before subducting into the interior ocean). These measurements capture the community-level oxygen consumption of phytoplankton and associated organic matter (including particulate and labile dissolved pools); however, they are limited in time and space. Using such approaches, some studies have suggested that $R_{-\Sigma O2:P}$ is close to 140 mol O_2/mol P (*20*, *21*). However, other studies propose a higher $R_{-\Sigma O2:P}$ of ~170 mol O_2/mol P, a value commonly adopted by Earth system models (*11*, *22*, *23*). A complication of this "top-down" method is that it relies on assumptions about water mass transport and the initial concentrations of preformed nutrient and O_2 concentrations. DeVries and Deutsch estimated water mass sources and their preformed values using a general circulation model constrained by biogeochemical tracers (i.e., an inverse model). By combining these estimates with observations of dissolved O_2 and phosphate, they inferred basin-scale variations in the $R_{-\Sigma O2:P}$, with higher values in the mid-latitude gyres and lower in equatorial and higher latitudes, and a global average of 147 mol O_2/mol P (*24*).

The variations in the $R_{-\Sigma O2:P}$ suggested by DeVries and Deutsch are broadly consistent with observed basin-scale variations in the C:P and N:P ratios of particulate organic matter collected in the ocean (*24*, *25*). These variations are driven by variable environmental conditions such as light, temperature, and dissolved nutrient concentrations through changes in phytoplankton community structure and intracellular adjustments of macromolecular composition (*25*–*28*). These observed latitudinal trends in the C:P and N:P ratios suggest that similar flexibility also exists in the H and the O content of cellular biomass. Nevertheless, we now lack an understanding of how the cellular content of H and O and the corresponding $R_{-\Sigma O2:P}$ and $R_{-\Sigma O2:C}$ vary at the global scale (*29*).

Here, we hypothesize that there are spatial variations in the H and O content of organic matter, as well as in $R_{-\Sigma O2:C}$ and $R_{-\Sigma O2:P}$,

Downloaded from https://www.science.org at University of Rhode Island on November 06, 2026

reflecting differences in the underlying macromolecular composition of the living phytoplankton pool driven by varying environmental conditions. For example, low-light conditions favor investment in light-harvesting proteins, which contain reduced N and CH_2 chains, over C storage macromolecules such as carbohydrates and lipids (Fig. 1) (*17*, *30*). Therefore, changes in environmental conditions can alter the complete elemental composition, including the H and the O content of freshly produced organic matter, and the amount of O_2 subsequently consumed during respiration.

Here, we address the following questions: (i) To what extent do the H and O content of marine particulate organic matter vary spatially, and why? (ii) To what extent do $R_{-\Sigma O2:P}$ and $R_{-\Sigma O2:C}$ vary spatially, and what are the key controlling processes? (iii) What is the global average C:H:N:O:P composition of particulate organic matter (including marine phytoplankton) and the corresponding global means $R_{-\Sigma O2:P}$ and $R_{-\Sigma O2:C}$? (iv) What is the sensitivity of the global ocean O_2 budget and the extent of hypoxic regions to plausible bounds of cellular allocation? (v) What is the sensitivity of regenerated C estimates via the biological pump (C^{soft}) to these bounds?

To address these questions, we simulated the macromolecular composition of phytoplankton in the global ocean, using a cellular allocation model (*31*, *32*) embedded within the Massachusetts Institute of Technology general circulation model (the MITgcm) (*33*) framework. The cellular allocation model integrates relationships between the major macromolecules of phytoplankton, such as proteins, carbohydrates, lipids, nucleic acids, and storage molecules, and environmental conditions, calibrated by extensive laboratory studies (Materials and Methods) (*27*, *28*, *34*). By assuming predefined elemental ratios of each macromolecule (Fig. 1B), we resolved the elemental composition of particulate organic matter, including the H and the O content of phytoplankton cells, its O_2 demand ($R_{-\Sigma O2:P}$) and total respiration quotient ($R_{-\Sigma O2:C}$).

RESULTS

Regional variations in total particulate organic matter composition

Our simulations predict latitudinal trends in the C:H:N:O:P composition of total particulate organic matter in the surface ocean, encompassing both phytoplankton cells and detrital particulate organic matter (Fig. 2). The latter is derived from phytoplankton and zooplankton biomass upon mortality, as well as from excess elements routed to

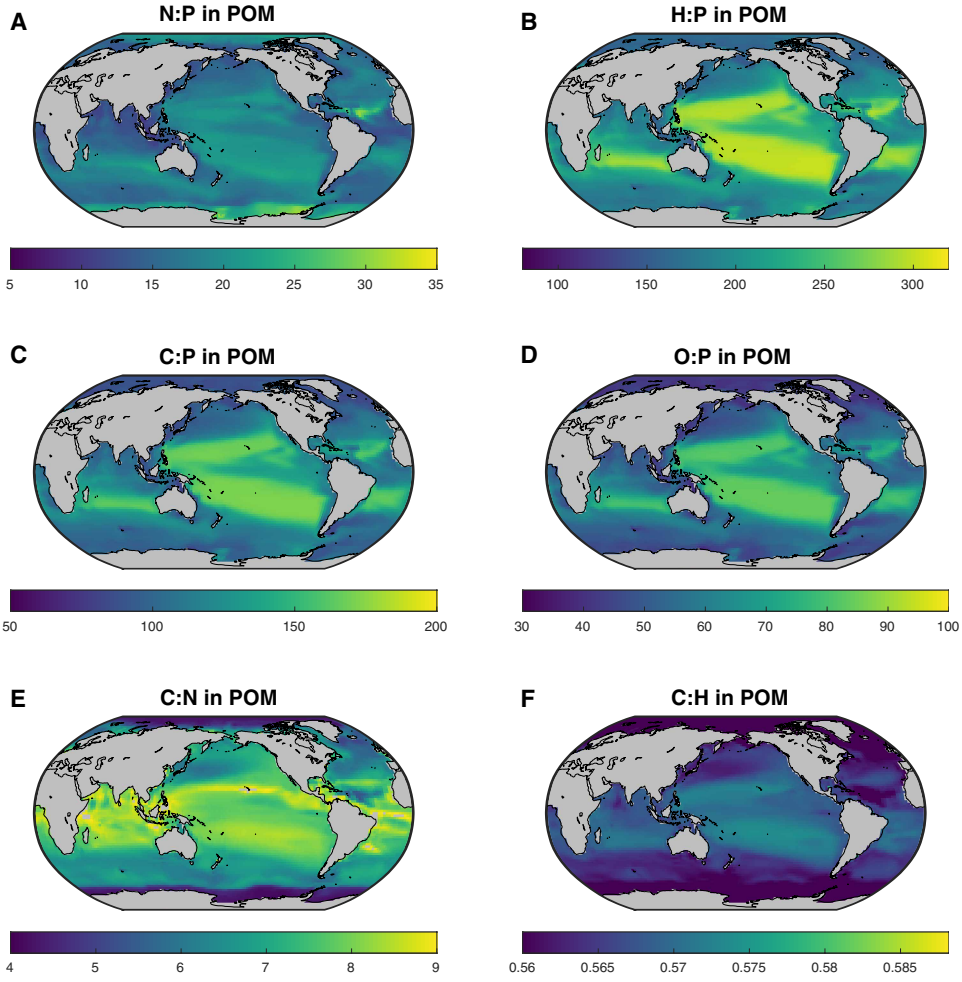

Fig. 2. Global trends in the C:H:N:O:P composition of total particulate organic matter encompassing phytoplankton and particulate organic matter. Maps show model-simulated, depth-integrated (0 to 170 m), annual mean molar ratios of (**A**) N:P, (**B**) H:P, (**C**) C:P, (**D**) O:P, (**E**) C:N, and (**F**) C:H in total particulate organic matter. The maps show 100-year means of the simulations.

Downloaded from https://www.science.org at University of Rhode Island on November 06, 2026

particulate organic matter due to selective grazing, under the assumption that grazers maintain elemental homeostasis (Supplementary Materials). Notably, we find that variations in modeled C:P, H:P, N:P, and O:P are primarily a result of changes in allocation to P storage (as polyphosphate) (fig. S1A), which, in turn, are linked to community composition because small phytoplankton have a lower phosphorus storage capacity than large phytoplankton (table S1) (*26*, *27*, *35*, *36*). Because phytoplankton in the ocean are limited mainly by light, iron, or nitrogen (*37*), with a limited areal-extent of phosphorus colimitation, phytoplankton often store phosphate until saturation. Therefore, in the nutrient-depleted (oligotrophic) subtropical gyres, where small phytoplankton with higher nutrient affinity and lower phosphate storage dominate (fig. S1), the C:P, H:P, N:P, and O:P ratios of total particulate organic matter are elevated (Fig. 2). On the other hand, in the subpolar regions and along the equator, where upwelling water enriches the supply of inorganic nutrients to the surface ocean, eukaryotic phytoplankton with higher maximum growth rates dominate (fig. S1). These larger cells have a higher phosphorus storage capacity (fig. S1A and table S1), so the N:P, C:P, O:P, and H:P ratios of total particulate organic matter in these regions are lower (Fig. 2).

Our simulations also suggest variations in modeled C:N and C:H of total particulate organic matter reflecting changes in cellular allocation to proteins (fig. S1C and Fig. 2). Proteins are rich in reduced N (Fig. 1B). Therefore, in locations where cellular investment in proteins is high, C:N and C:H of total particulate organic matter are lower (Fig. 2, E and F). This typically occurs in nutrient-rich, low-light conditions at high latitudes (fig. S1C) (*27*, *28*, *38*, *39*) where cells invest more in both light-harvesting and biosynthetic proteins, enabling the energy-capture and synthetic capacity to meet the faster growth (*28*, *40*) facilitated by higher nutrient supply rates. Higher investment in photosynthetic proteins also drives low C:N in the western tropical North Atlantic, where our model simulates higher phytoplankton biomass at 150-m depth due to surface nutrient depletion (fig. S2). Phytoplankton growing under sea-ice in the polar regions invest even further in photosynthetic proteins, and their C:N and C:H are consequently very low (Fig. 2, E and F). In subtropical oligotrophic gyres, where phytoplankton experience high-light and low-nutrient conditions, their mass-specific relative growth rates are lower, and excess light energy is stored in carbon-rich storage macromolecules such as lipids and carbohydrates (fig. S1, B and D). Consequently, our simulations predict higher C:N and C:H ratios in these regions (Fig. 2, E and F).

The modeled C:P and N:P of total particulate organic matter qualitatively capture the large-scale spatial patterns of global observations, including the higher values in subtropical oligotrophic regions and the lower values in equatorial and high-latitude regions, although the model underestimates the full range of observed variability (Fig. 3, A and B, and fig. S3, A and B). The relatively low variability in the modeled C:P and N:P ratios compared with that in observations, in part, reflects the limited biogeographic distribution of phytoplankton groups across each ecoprovince (fig. S3). This is primarily due to the model's inclusion of only two phytoplankton size classes, each with specific P storage capacities (Materials and Methods). In contrast, the relatively high variability in the model C:N reflects variability over depth in the cellular protein content. Overall, the basin-scale signal in the observed C:N is small relative to its local variability, making a quantitative assessment of model skill in capturing observed patterns challenging (Fig. 3C and fig. S3C). Nevertheless, the model successfully reproduced observed patterns in protein allocation in the North Pacific and Southern Ocean (*28*, *40*, *41*), suggesting that the underlying mechanisms driving the modeled patterns are robust.

Global variations in the oxygen demand and respiration quotient of total particulate organic matter

Our model simulations predict global variations in the oxygen demand ($R_{-\Sigma O2:P}$) ranging from 110 to 280 mol O_2/mol P, with higher values in the mid-latitude oligotrophic gyres and lower values at higher latitudes (Fig. 4C). Our mechanistic model results fall within the uncertainty envelope of $R_{-\Sigma O2:P}$ estimated using an ocean circulation model constrained by observations (i.e., an "inverse" model) and measurements of dissolved nutrient ratios (shown as dashed line in Fig. 4D) (*24*), pleasingly showing correspondence between "bottom-up" and "top-down" approaches.

To understand the drivers of this variability, we decompose the oxygen demand into three contributions. Our mechanistic model reveals that variations in oxygen demand primarily reflect changes in the ratio of oxidized organic C to P (i.e., the C:P of organic matter; purple area in Fig. 4D). Variations in the O_2 demand are also influenced, to a lesser extent, by oxidation of organic reduced N to nitrate (i.e., the N:P of organic matter; green area in Fig. 4D). Both C:P and N:P are mostly driven by phytoplankton cell-size–specific P storage, whereas N:P is also influenced to a lesser extent by protein content. A smaller contribution comes from excess H associated with variations in lipid and protein content of the organic matter (yellow area in Fig. 4D; Materials and Methods). Because the model represents only two phytoplankton size classes with size-class–specific P storage capacity and restricted biogeographic distribution, variations in modeled oxygen demand are limited. Increasing taxonomic resolution would likely increase variability in the modeled oxygen demand, bringing it closer to observations.

We also find that there are global variations in total respiration quotient ($R_{-\Sigma O2:C}$) of organic matter between 1.3 and 1.5, with a biomass-weighted global mean of 1.40 (Fig. 4B). $R_{-\Sigma O2:C}$ is lowest in the subtropical gyres. Here, phytoplankton invest a high proportion of their biomass in carbohydrates, which are relatively oxidized forms of organic matter (fig. S1B and Fig. 1B). In contrast, $R_{-\Sigma O2:C}$ is highest at high latitudes where phytoplankton are mainly composed of proteins, which are a more reduced form of organic matter and have $R_{-\Sigma O2:C}$ of 1.59 (fig. S1C and Fig. 1B). Our model simulations also suggest that $R_{-\Sigma O2:C}$ increases with depth within the euphotic zone (*42*) as phytoplankton invest more in photosynthetic proteins in response to diminishing light availability (Fig. 5 and fig. S4).

Our model simulations further suggest that the modeled partial respiration quotient $R_{-O2:C}$ (see Box 1), which reflects respiration of organic matter to ammonia, is nearly spatially constant at $R_{-O2:C} \approx 1.1$. $R_{-O2:C}$ mirrors the reduction/oxidation state of C in the cell. For example, carbohydrates are considered more oxidized, as they contain more C—O bonds relative to lipids that are more reduced and enriched in C—H bonds. Because we assume that cellular C storage is partitioned equally between carbohydrates and lipids, they share similar geographic distributions (fig. S1, B and D). As a result, the C oxidation state and the $R_{-O2:C}$ are essentially uniform in our model. This implies that most of the global variability in the modeled total respiration quotient ($R_{-\Sigma O2:C}$) arises from changes in the reduced nitrogen content, primarily associated with cellular allocation to proteins (fig. S1C).

Downloaded from https://www.science.org at University of Rhode Island on November 06, 2026

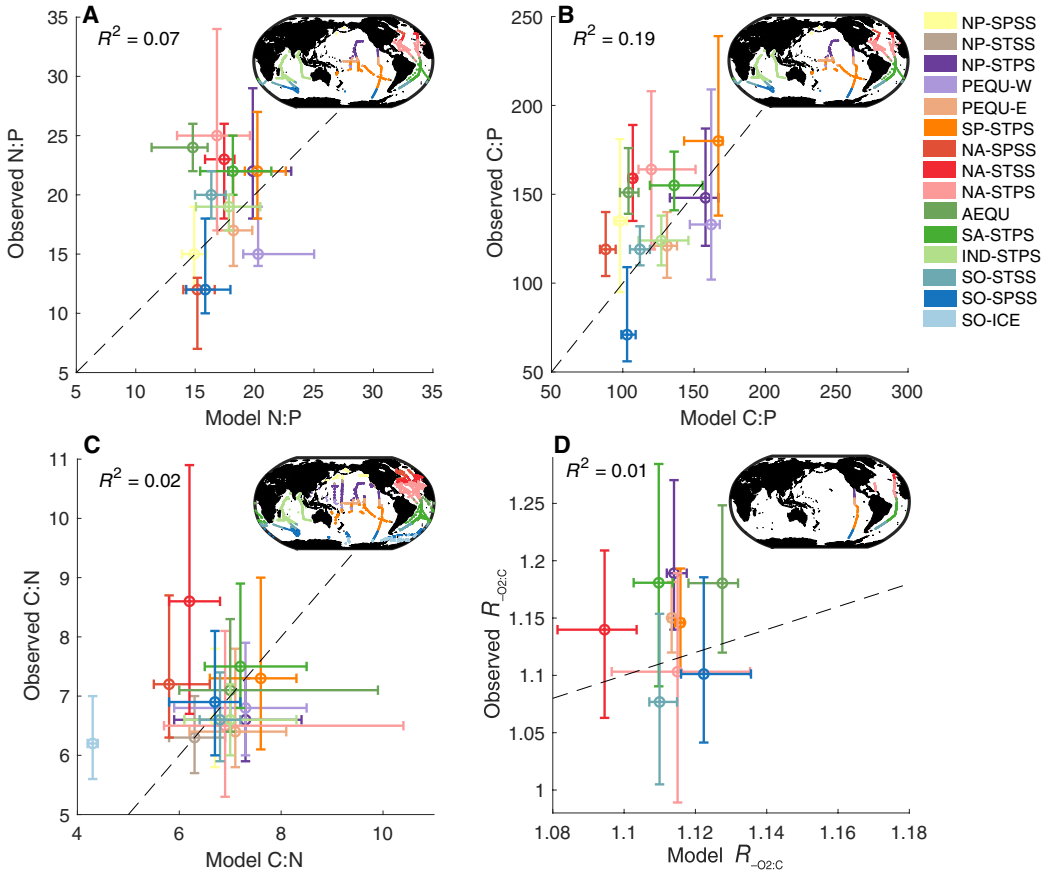

Fig. 3. Comparison of modeled and observed elemental ratios of particulate organic matter. Panels show linear regression between the medians of modeled and observed (**A**) N:P, (**B**) C:P, (**C**) C:N, and (**D**) partial respiration quotient ($R_{-O2:C}$) that does not account for the O_2 consumed during nitrification (Box 1). The observed data are clustered by different ecological provinces classified from observed SST, chlorophyll a concentrations, ice cover, and maximum mixed layer depth (*81*). The error bars extend to the 25th and 75th percentiles of the model and observations. R^2 indicates the goodness of the linear fit. Observational data represent open-ocean samples from the upper 170 m (*25*, *42*, *44*, *82*). The model output represents the 100-year mean of particulate organic matter (phytoplankton plus particulate organic matter) in the upper 170 m. Modeled and observed error bars reflect variability across depth and ecoprovinces. Only ecoprovinces with more than 13 observations are shown. Regions: NP-ICE, North Pacific Ice; NP-SPSS, North Pacific Subpolar Seasonally Stratified; NP-STSS, North Pacific Subtropical Seasonally Stratified; NP-STPS, North Pacific Subtropical Permanent Stratified; PEQU-W, West Pacific Equatorial; PEQU-E, East Pacific equatorial; SP-STPS, South Pacific Subtropical Permanent Stratified; NA-SPSS, North Atlantic Subpolar Seasonally Stratified; NA-STSS, North Atlantic Subtropical Seasonally Stratified; NA-STPS, North Atlantic Subtropical Permanent Stratified; AEQU, Atlantic Equatorial; SA-STPS, South Atlantic Subtropical Permanent Stratified; IND-STPS, Indian Ocean Subtropical Permanent Stratified; SO-STSS, Southern Ocean Subtropical Seasonally Stratified; SO-SPSS, Southern Ocean Subpolar Seasonally Stratified; SO-ICE, Southern Ocean Ice.

Available observations include measurements only of partial respiration quotient (i.e., $R_{-O2:C}$), as the current method does not oxidize ammonia to nitrate (*42*–*44*). Our predicted $R_{-O2:C}$ generally fall within the uncertainty range of available measurements (Fig. 3D and fig. S3D), although the higher variability on the spatial signal and the limited data make a robust, quantitative assessment still challenging.

Linear relationships between elemental composition, the total respiration quotient, and oxygen demand

Our mechanistic model enables us to identify linear relationships among elemental ratios, the total respiration quotient, and oxygen demand in total particulate organic matter. Specifically, we find an inverse linear relationship between the C:N ratio of organic matter and the total respiration quotient [$R_{-\Sigma O2:C} = -0.026 \times C{:}N + 1.565$, coefficient of determination (R^2) = 0.72; Fig. 6A] as higher protein content drives lower C:N ratios while simultaneously increasing $R_{-\Sigma O2:C}$ due to the additional oxygen required to oxidize reduced N in proteins. This relationship is consistent with the theoretical framework that derived analytical limits on $R_{-\Sigma O2:C}$ as a function of C:N and the carbohydrate-to-lipid ratio (*45*). N:P shows no clear relationship with the $R_{-\Sigma O2:C}$ (R^2 = 0.06; Fig. 6C). We further find that the partial respiration quotient ($R_{-O2:C}$), which shows only minor spatial variability (1.1 to 1.15), does not correlate with the C:N, N:P, or C:P of organic matter ($R^2 \leq 0.03$; fig. S5).

We further find that the total oxygen demand ($R_{-\Sigma O2:P}$, mol O_2/mol P) is positively related to the N:P ($R_{-\Sigma O2:P} = 11.0 \times N{:}P - 13.90$, R^2 = 0.84) and C:P ($R_{-\Sigma O2:P} = 11.0 \times C{:}P + 7.66$, R^2 = 0.9965) of organic matter (Fig. 6, B and D). The notable relationship between the C:P and $R_{-\Sigma O2:P}$ indicates that C:P alone is sufficient to predict the total oxygen demand of organic matter decomposition. This follows directly from the fact that $R_{-\Sigma O2:P}$ is a direct multiplicative product of C:P and $R_{-\Sigma O2:C}$: $R_{-\Sigma O2:P} = (R_{-\Sigma O2:C}) \times (C{:}P)$. Because the variability in $R_{\Sigma\text{-}O2:C}$ is much narrower (1.3 to 1.5) relative to variability in C:P (80 to 200), the much larger relative variability in C:P dominates

Downloaded from https://www.science.org at University of Rhode Island on November 06, 2026

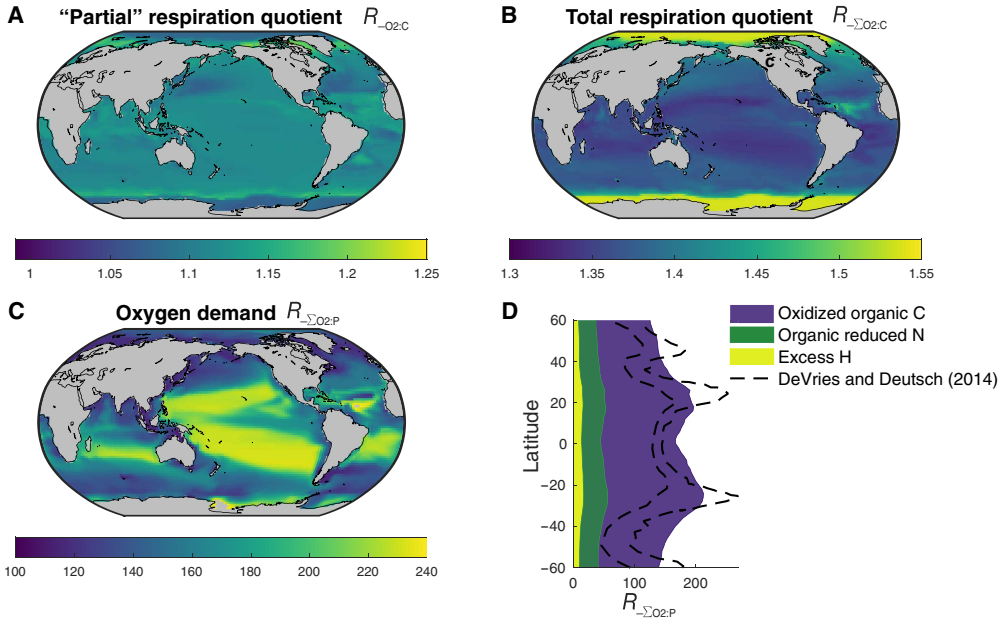

Fig. 4. Oxygen demand and respiration quotient in particulate organic matter. Depth-integrated (0 to 170 m), annual mean model results of (**A**) partial respiration quotient that does not account for the O_2 consumed during nitrification ($R_{-O2:C}$, mol O_2/mol C), (**B**) total respiration quotient ($R_{-\Sigma O2:C}$, mol O_2/mol C), and (**C**) O_2 demand ($R_{-\Sigma O2:P}$, mol O_2/mol P). (**D**) Modeled latitudinal trend in $R_{-\Sigma O2:P}$ for the oxidation of CH_2O (i.e., the C:P of organic matter; dark-purple area), organic reduced N (i.e., the N:P of organic matter; green area), and excess H (yellow area) estimated by this study, along with estimated (dashed black lines) values from DeVries and Deutsch (*24*). Note that the scale of the colorbars in (C) and (D) is different.

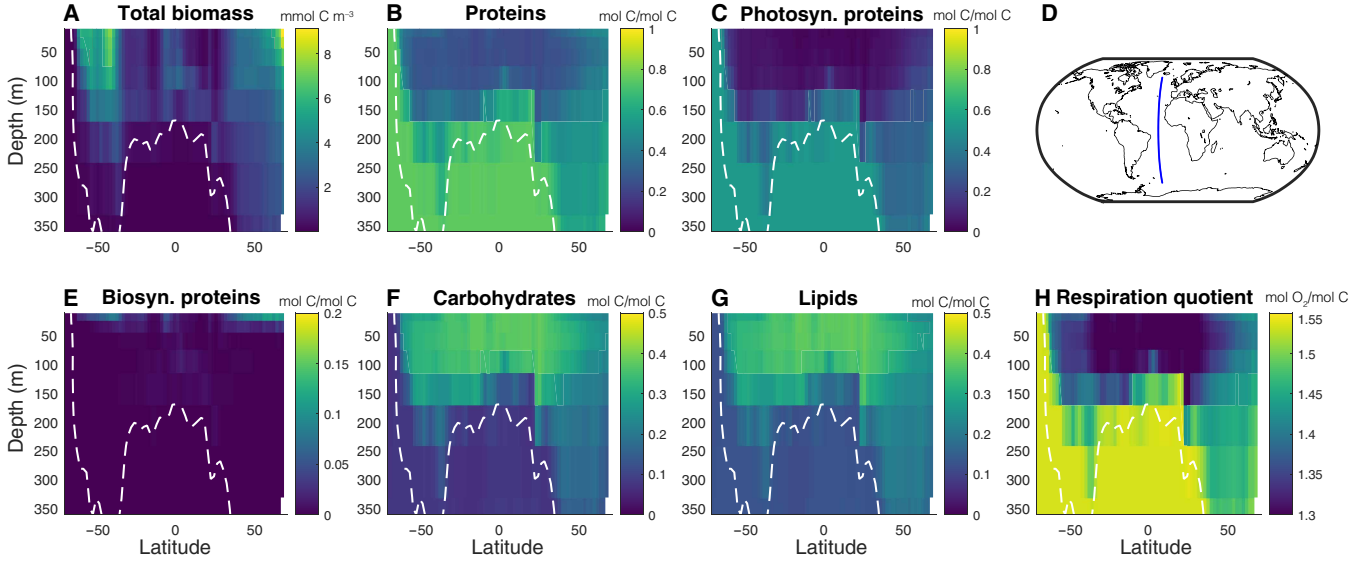

Fig. 5. Depth transect of phytoplankton biomass, macromolecular composition, and total respiration quotient in the Atlantic. Panels show modeled phytoplankton (**A**) biomass (mmol C/m^3), and cellular allocation (mol C/mol C) to (**B**) total protein, (**C**) photosynthetic proteins, (**E**) biosynthetic proteins, (**F**) carbohydrates, (**G**) lipids, and (**H**) the corresponding total respiration quotient ($R_{-\Sigma O2:C}$; mol O_2/mol C). (**D**) The transect on a global map. Dashed white lines in (A) to (C) and (E) to (H) indicate the threshold where biomass is lower than 0.1 mmol C/m^3.

the variability in $R_{\Sigma\text{-}O2:P}$. This further implies that the classical RKR assumption of a fixed H and O content of a phytoplankton cell introduces a relatively modest error in oxygen demand estimates compared with the assumption of a fixed C:P ratio. Improving the representation of C:P variability in biogeochemical models may therefore be more impactful than simulating variations in the total respiration quotient.

Global average elemental composition of a phytoplankton cell

We found the emergent, weighted global-average phytoplankton composition of $C_{107}H_{190}N_{16}O_{53}P$, with $R_{-\Sigma O2:P}$ of 149 mol O_2/mol P and a $R_{-\Sigma O2:C}$ of 1.40 mol O_2/mol C (Table 1). This composition results from a simulated global, annual mean composition of phytoplankton cells consisting of 41% proteins, 27% lipids, 25% carbohydrates,

Downloaded from https://www.science.org at University of Rhode Island on November 06, 2026

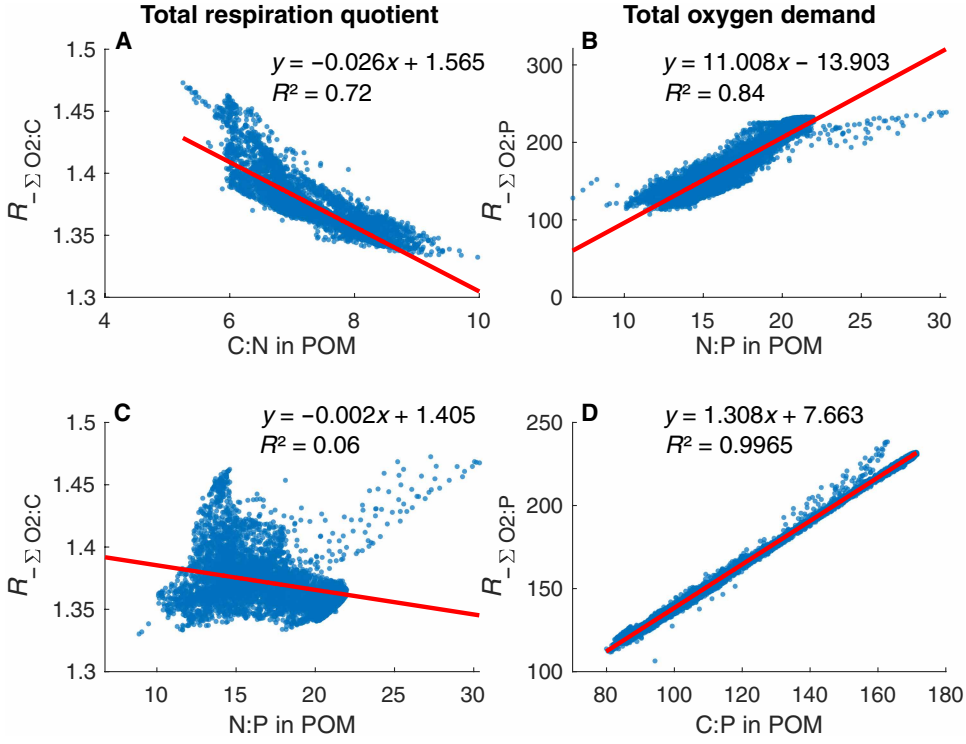

Fig. 6. Linear regressions between elemental ratios, total respiration quotient, and oxygen demand in total particulate organic matter (phytoplankton and detrital POM). (**A**) C:N ratio versus the total respiration quotient ($R_{-\Sigma O2:C}$, mol O_2/mol C), (**B**) N:P ratio versus the total oxygen demand ($R_{-\Sigma O2:P}$, mol O_2/mol P), (**C**) N:P ratio versus $R_{-\Sigma O2:C}$ (mol O_2/mol C), and (**D**) C:P ratio versus the $R_{-\Sigma O2:P}$ (mol O_2/mol P). Values are biomass-weighted means over the upper 170 m. R^2 denotes the coefficient of determination of the linear fit.

Table 1. Average phytoplankton chemical formula and associated oxygen demand. Average chemical formula and oxygen demand ($R_{-\Sigma O2:P}$) of production and heterotrophic respiration of marine phytoplankton derived from the model simulations, based on the simulated global mean macromolecular composition of 41% proteins, 27% lipids, 25% carbohydrates, 5% N storage, 1.5% chlorophyll a, and 0.5% nucleic acids (mol C/mol C).

Chemical formula*	**$107CO_2 + 16HNO_3 + H_3PO_4 + 85.5H_2O \rightleftarrows C_{107}H_{190}N_{16}O_{53}P + 149O_2$**
Oxygen demand ($R_{-\Sigma O2:P}$)	149
Total respiration quotient ($R_{-\Sigma O2:C}$)	1.40
Oxygen consumption of CH_2O (%)	72% (107 of 149)
Oxygen consumption of reduced N (%)	21% (32 of 149)
Oxygen consumption of excess H (%)	7% (10 of 149)

*For comparison, the classical RKR formula (*16*) assumes the following formula: $106CO_2 + 16HNO_3 + H_3PO_4 + 122H_2O \rightleftarrows C_{106}H_{263}N_{16}O_{110}P + 138O_2$, with $R_{-\Sigma O2:P}$ of 138 mol O_2/mol P and $R_{-\Sigma O2:C}$ of 1.30 mol O_2/mol C, where 77% of the O_2 consumption is due to oxidizing CH_2O and 23% is due to the oxidation of organic N (see main text).

5% N storage (as cyanophycin), 1.5% chlorophyll, and 0.4% nucleic acids (DNA and RNA) (mol C/mol C). Our estimates of average H and O content are lower than the classical RKR formula due to the explicit inclusion of lipids and proteins in our simulations, which are more reduced than carbohydrates, but which were not accounted for in the classical approach (*16*). Our prediction of global mean $R_{-\Sigma O2:P}$ oxygen demand of 149 mol O_2/mol P closely matches the global average of 147 mol O_2/mol P inferred from top-down approaches DeVries and Deutsch (*24*) as well as the value estimated by Laws and Anderson from average cellular composition (*18*, *19*). This first-principles value is higher than the $R_{-\Sigma O2:P} = 138$ implied by the RKR formula but lower than the value of 170, commonly used in biogeochemical models (*12*).

We explored how much of the O_2 consumption (149 mol O_2/mol P) is due to (i) the oxidation of organic C as carbohydrates (CH_2O); (ii) the oxidation of organic N (mainly associated with proteins and N-storage molecules as cyanophycin) to nitrate; and (iii) excess of H due to the inclusion of other macromolecules that are more reduced; mainly proteins and lipids (Materials and Methods). Our model simulations suggest that 72% (107 of 149) of the O_2 demand is due to the oxidation of C in the form of CH_2O, 21% (32 of 149) is due to the oxidation of organic N to nitrate, and 7% (10 of 149) is due to the oxygenation of excess of H associated with variations in the lipid and proteins content (Table 1). In comparison, the classical RKR equation assumes that 77% (106 of 138) of the O_2 consumption is due to oxidizing CH_2O, and the remaining 23% (32 of 138) is due to the oxidation of organic N to nitrate. Explicitly representing proteins and lipids reveals an additional, nonnegligible O_2 sink.

The impact of variations in $R_{-\Sigma O2:C}$ on the global oxygen budget

There are many regions in the ocean where O_2 is too low to sustain aerobic metabolic activity, favoring alternate microbial electron acceptors and the exclusion of aerobic metazoans. These hypoxic zones

Downloaded from https://www.science.org at University of Rhode Island on November 06, 2026

are now expanding, likely due to changes related to thermal solubility, ventilation, and primary productivity (*46*–*49*). Alongside these trends, changes in the underlying macromolecular composition of phytoplankton may occur, which can either mute or exacerbate the impact of warming (*50*). For example, under nitrate-poor conditions, cells may reduce their protein levels and increase investments in carbohydrates and/or lipids (*17*, *40*), changing their total respiration quotient, $R_{-\Sigma O2:C}$. Here, we ask: What is the sensitivity of the global ocean O_2 inventory and the extent of the ocean hypoxic zones to plausible variations in cellular allocation?

To diagnose the impact of varying $R_{-\Sigma O2:C}$ on the oceanic O_2 budget, we conducted two model simulations (Materials and Methods). In these simulations, the nutrients, ecosystem, and corresponding primary productivity were comparable (fig. S6), and $R_{-\Sigma O2:C}$ was the sole variable. In the first experiment, we set $R_{-\Sigma O2:C}$ to a spatially constant of 1.3. This value is the lowest $R_{-\Sigma O2:C}$ simulated by our model, representing subtropical phytoplankton with relatively high carbohydrate content. In the second experiment, we prescribed $R_{-\Sigma O2:C}$ to 1.5. This is the highest $R_{-\Sigma O2:C}$ simulated by our model, representing high-latitude phytoplankton with high protein content (Fig. 4B). We argue that these values represent the plausible bounds of modeled phytoplankton physiological adaptation to varying environmental conditions, noting that $R_{-\Sigma O2:C}$ values outside this range have been observed in oceanic samples (*42*–*44*).

To test the impact on the global O_2 inventory, we simulated the biogeochemical tracers for 2000 years, until they reached a quasi-steady state and were in reasonable agreement with modern-ocean observations (figs. S6 to S9; Materials and Methods). Our simulations indicate that changing $R_{-\Sigma O2:C}$ from 1.3 to 1.5, the total O_2 inventory shrinks by 11% due to higher O_2 consumption rates after 2000 years of simulation. As a response, the volume of the hypoxic regions where $O_2 < 62$ μM increases by a factor of 1.75 and the volume of the hypoxic regions where $O_2 < 25$ μM increases by a factor of 2.8 (Table 2). The sensitivity of ocean volume to the total respiration quotient at $[O_2] < 25$ μM is due to the steep slope of the cumulative distribution function of O_2 concentration, where a slight shift leads to a substantial change in hypoxic volumes (fig. S10). Although not explicitly resolved in this model (see below), such an increase in the extent of the hypoxic regions would likely increase denitrification rates and the loss of nitrate through anaerobic respiration of organic matter.

The impact of variations in $R_{-\Sigma O2:C}$ on estimates of regenerated carbon via biological respiration

In the previous section, we demonstrated the sensitivity of the global oxygen budget to respiration quotient at fixed rates of primary productivity. In this section, we assess how spatial variations in respiration quotient influence estimates of regenerated organic C under fixed oxygen utilization (i.e., the apparent biological C "soft tissue pump"; C^{soft}). Such estimates of regenerated organic C are intrinsically connected to O_2 consumption and are commonly inferred from apparent oxygen utilization (AOU) using a constant respiration quotient. Our goal is to place theoretical limits on the C^{soft} inventory, a crucial component of the oceanic C cycle that plays an important role in the ocean-atmosphere carbon partitioning (*51*–*53*).

First, we calculate C^{soft} by dividing AOU estimates diagnosed from observations (*51*, *54*) with the spatially variable $R_{-\Sigma O2:C}$ obtained in our study (Fig. 7A). We note that AOU estimates assume a full equilibration of O_2 across the air-sea interface and do not include processes that can drive surface O_2 disequilibrium, such as surface heat exchange, sea ice cover, and short exposure time of upwelled oxygen-depleted deep waters (*55*). Nevertheless, the error in AOU due to disequilibrium in O_2 will be almost identical in both variable and constant respiration quotient simulations because it depends on other, common process and thus will factor out when comparing globally integrated C^{soft} between these simulations

We find that 1515 Pg C is the apparent biological "soft tissue pump" added to the ocean via remineralization of organic carbon (C^{soft}). The added respired carbon follows patterns of AOU; it is highest in the equatorial Atlantic at 500- to 600-m depth, and in the Pacific, northward to the equator at 1000- to 2000-m depth (Fig. 7A). These patterns are consistent with previous assessments (*51*, *52*, *56*, *57*). Similarly, we calculated C^{soft} using spatially homogeneous $R_{-\Sigma O2:C}$ values of 1.3 and 1.5, representing the plausible bounds of modeled physiological adaptation discussed earlier and the global average $R_{-\Sigma O2:C} = 1.40$. We compare these C^{soft} estimates with the baseline case of a spatially variable $R_{-\Sigma O2:C}$ from our study.

We find that C^{soft} estimates are sensitive to the choice of $R_{-\Sigma O2:C}$ (Fig. 7, B to D). In total, 1598 Pg C is estimated with spatially constant $R_{-\Sigma O2:C} = 1.3$ as more C is regenerated per O_2 consumed. Conversely, C^{soft} estimated with spatially fixed $R_{-\Sigma O2:C}$ of 1.5 is 1385 Pg C as less C is regenerated per O_2 consumed (Table 3 and Fig. 7B). This 213 Pg C difference can introduce ~15% error when estimating globally integrated C^{soft}. C^{soft} estimated using a spatially fixed $R_{-\Sigma O2:C} = 1.40$ is 1484 Pg C, i.e., 2% lower than the spatially variable $R_{-\Sigma O2:C}$ (Table 3).

To provide a finer resolution on the regions where the assumption of a constant $R_{-\Sigma O2:C}$ may result in the greatest mismatch, we further compare the C^{soft} estimated using a spatially constant $R_{-\Sigma O2:C} = 1.40$, which is the global average (Table 1), and the spatially variable $R_{-\Sigma O2:C}$ obtained by our study. Assuming a mean $R_{-\Sigma O2:C}$ of 1.40 tends to overestimate the respiration quotient compared with modeled values, particularly between latitudes 50°S and 50°N while underestimating $R_{-\Sigma O2:C}$ at higher latitudes (fig. S11).

Table 2. The sensitivity of the global oxygen cycle to $R_{-\Sigma O2:C}$.

	O_2 inventory* (Tmol)	Mean O_2* (μM)	Hypoxic zone volume* [$O_2 < 62$] (1×10^7 km^3)	Hypoxic zone volume* [$O_2 < 25$] (1×10^7 km^3)
$R_{-\Sigma O2:C} = 1.3$	2.18×10^5	193	16.2	3.7
Variable $R_{-\Sigma O2:C}$†	2.07×10^5	185	21.8	7.5
$R_{-\Sigma O2:C} = 1.5$	1.95×10^5	178	28.4	10.7

*After 2000 years of simulation. †Spatially variable total respiration quotient ($R_{-\Sigma O2:C}$), shown in Fig. 4B.

Downloaded from https://www.science.org at University of Rhode Island on November 06, 2026

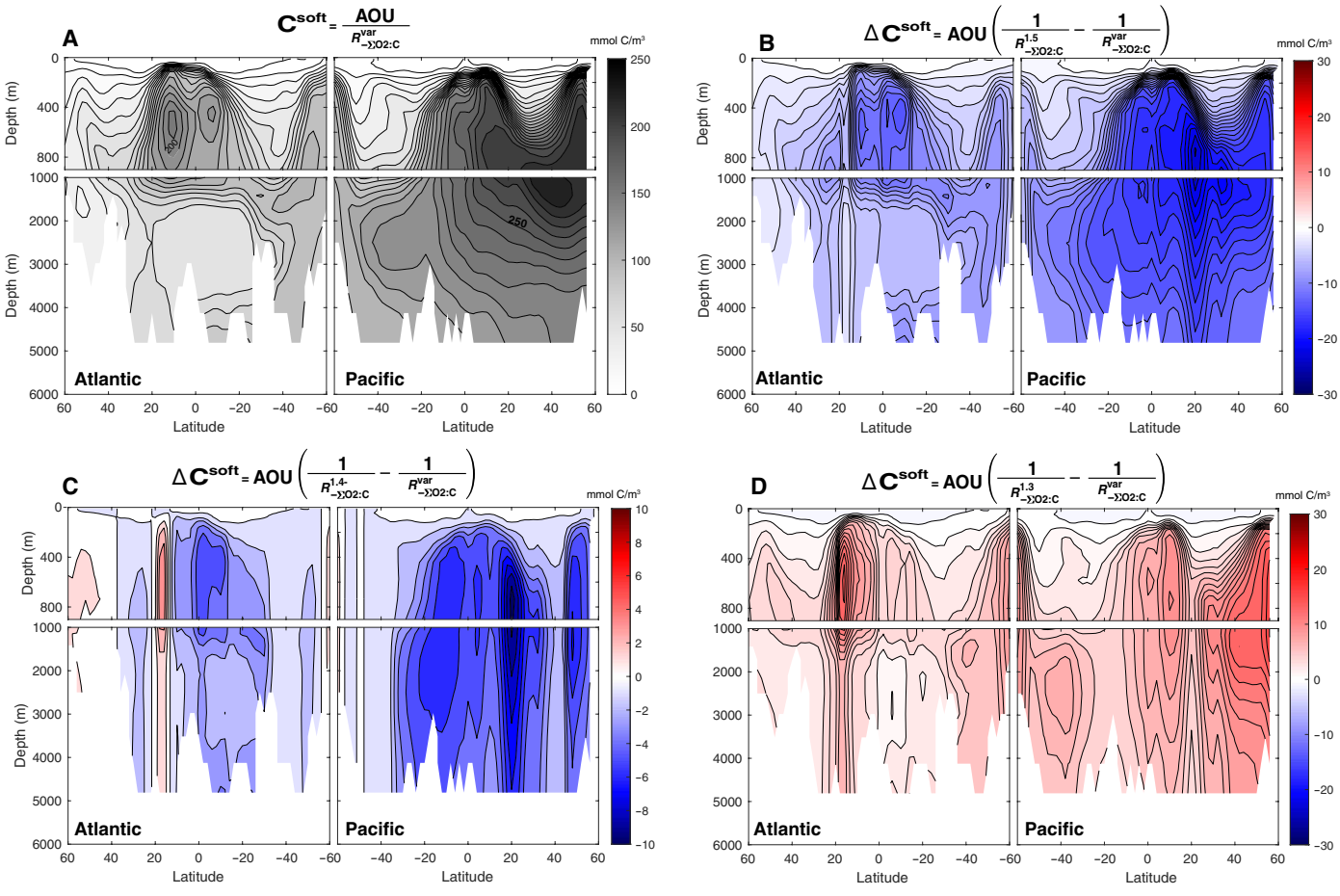

Fig. 7. Atlantic and Pacific meridional sections of regenerated carbon. (**A**) Estimates of regenerated inorganic carbon via respirations (C^{soft}; mmol C/m^3) calculated from AOU (mmol O_2/m^3) diagnosed from observations of dissolved O_2, temperature and salinity (*54*). (**B** to **D**) Difference in C^{soft} estimated assuming spatial uniform $R_{-\Sigma O2:C}$ values of 1.5 (B), 1.4 (C) and 1.3 (D) relative to estimates using the spatially variable $R_{-\Sigma O2:C}$ (Fig. 4B).

Table 3. The sensitivity of regenerated carbon estimates (C^{soft}) to $R_{-\Sigma O2:C}$.

	C^{soft} (Pg C)*	ΔC^{soft} (Pg C)‡	ΔC^{soft} (%)‡
Variable $R_{-\Sigma O2:C}$†	1515	–	–
$R_{-\Sigma O2:C} = 1.3$	1598	+83	+5.5%
$R_{-\Sigma O2:C} = 1.4$	1484	−31	−2.0%
$R_{-\Sigma O2:C} = 1.5$	1385	−130	−8.6%

*C^{soft} is calculated from AOU (*54*) and $R_{-\Sigma O2:C}$. †Variable total respiration quotient presented in Fig. 4B. ‡Difference in C^{soft} estimated assuming spatial uniform $R_{-\Sigma O2:C}$ values of 1.3, 1.4, and 1.5 relative to estimates using the spatially variable $R_{-\Sigma O2:C}$.

Consequently, when a mean $R_{-\Sigma O2:C}$ is assumed, C^{soft} tends to be underestimated in the mid-latitudes (relative to estimates using spatially variable $R_{-\Sigma O2:C}$) and overestimated at high latitudes (Fig. 7C). An exception is in the western tropical North Atlantic, where $R_{-\Sigma O2:C}$ is relatively high due to low C:N and C:H values. There, the assumption of a fixed $R_{-\Sigma O2:C} = 1.40$ underestimates $R_{-\Sigma O2:C}$ values and, therefore, overestimates C^{soft} (Fig. 7C). We note that, given limited observational coverage, the spatial trends in $R_{-\Sigma O2:C}$ are derived from first principles, and both this spatial pattern and the corresponding C^{soft} estimates have yet to be empirically confirmed.

DISCUSSION

While previously published models have focused on resolving dynamic C:N:P in freshly produced organic matter (*36*, *38*, *58*, *59*), we have here included explicit accounting for H and the O, i.e., the elemental C:H:N:O:P of organic matter. We achieved this by integrating a cellular allocation model into a global ocean model, which explicitly resolves relationships constrained by experimental work between phytoplankton's macromolecular composition and environmental conditions (*27*, *34*, *60*). Using this method, we also estimated the O_2 demand ($R_{-\Sigma O2:P}$) and total respiration quotient ($R_{-\Sigma O2:C}$) of marine

Downloaded from https://www.science.org at University of Rhode Island on November 06, 2026

phytoplankton in the global ocean, from first principles, i.e., from the biochemical composition of a phytoplankton cell. Our work extends the bottom-up approach of Laws and Anderson (*18*, *19*), who estimated phytoplankton's oxidation state from average biochemical composition of a cell. Here, we explicitly resolve the effect of spatial patterns in the oxidation state of organic matter.

We find global-scale patterns in the elemental composition and O_2 demand, as a result of acclimation and adaptation to underlying variations in environmental conditions. We found that modeled C:P, N:P, and $R_{-\Sigma O2:P}$ are driven by variations in phytoplankton P-storage capacity, whereas modeled C:N, C:H, and $R_{-\Sigma O2:C}$ mostly resemble allocation to proteins. Our approach indicates that the ratio of dissolved O_2 to regenerated nutrients is not fixed and can be predicted from first principles, providing a mechanistic link between phytoplankton biochemical properties (bottom-up) and large-scale biogeochemical patterns (top-down).

These global variations give rise to a weighted global-average chemical formula of production and heterotrophic respiration of marine phytoplankton cells of $C_{107}H_{190}N_{16}O_{53}P + 149O_2 \rightarrow 107CO_2 + 16HNO_3 + H_3PO_4 + 85.5\ H_2O$. This formula suggests that freshly produced phytoplankton cells contain less H and O and, therefore, are more reduced than the classical RKR equation (Eq. 1). As a result, we obtained higher estimates than the classical RKR equation for $R_{-\Sigma O2:P}$ and $R_{-\Sigma O2:C}$, specifically 149 mol O_2/mol P and 1.40 mol O_2/mol C, respectively.

The resulting global-average $R_{-\Sigma O2:P}$ and its variations are consistent with expectations derived from completely different data sets, i.e., from an inverse model constrained by global-scale ocean nutrient distributions (*24*). The convergence of bottom-up and top-down models is pleasing, and the mechanistic, forward model presented here provides additional insight into the processes underlying the patterns. The correspondence for present day distributions also gives confidence in the application of this forward model for predictive applications that are not accessible to the inverse modeling approach.

Although the cellular allocation model captures global mean values and basin-scale trends effectively (fig. S3), it does not account for the full range of variability observed in the elemental composition of organic matter collected in the field (Fig. 3). This unresolved variability likely arises from several factors, including: (i) the sparse and stochastic nature of the observations, (ii) the coarser resolution of our simulations relative to the true spatial and temporal variability of oceanographic conditions, and (iii) the greater complexity of real biogeochemical and ecological processes that are not represented in the model. One example of this reduced complexity is our model's omission of preferential remineralization of specific macromolecules or elements in organic matter within the water column. The absence of preferential degradation, along with the other simplifications discussed below, likely contributes to the model's underestimation of field-observed variability.

The cellular allocation model is built upon basic knowledge from extensive laboratory experimental work (*17*, *61*, *62*). Nevertheless, some gaps in our knowledge remain, which may introduce uncertainties into our results. In particular, due to our focus on macromolecular allocation and steady-state integrations, we have not incorporated a fully dynamic nitrogen cycle, shaped by the balance between nitrogen fixation and denitrification. In part, this is because the cellular allocation model resolves only two phytoplankton classes (i.e., "small" and "large") and does not capture the full taxonomic diversity of the phytoplankton community. For instance, the model does not resolve N_2-fixing organisms, which allocate a substantial fraction of cellular N to nitrogenase, have distinct trace-metal requirements, and may produce compounds that are not represented in the current macromolecular framework [e.g., phosphonates; (*63*)]. N_2 fixers, which mostly occupy the warm oligotrophic regions (*64*), have high C:P and N:P (*65*). Their activity may draw down phosphorus available to non–N_2-fixing phytoplankton, potentially increasing the C:P and N:P of nonfixers. Additionally, N_2-fixation machinery is protein rich (*66*) and has a high total respiration quotient relative to the average cell found in our study (Fig. 1B). Therefore, inclusion of N_2 fixers may increase spatial variability in elemental ratios and the total respiration quotient.

Another key limitation of the model is the use of a fixed, average composition for each macromolecular pool, despite substantial biochemical diversity in nature. This is particularly true for lipids, which vary across phytoplankton groups, environmental conditions, and the diel cycle (*67*–*69*). For example, under low P concentrations, phytoplankton can substitute phospholipids with sulfur- and nitrogen-containing membrane lipids (*70*). However, a small number of highly abundant lipids account for a disproportionate share of the total cell mass (*69*), and their total respiration quotient do not differ substantially (table S3), limiting the impact of different lipid production on the total respiration quotient. Increasing both the taxonomic and biochemical diversity will likely increase the variability among modeled stoichiometries and represent an important next step toward understanding patterns of respiration in the ocean (*71*, *72*).

We further show that changes in cellular composition and the resulting shifts in cell respiration quotient affect global O_2 concentrations and the extent of the hypoxic zones. Therefore, alterations in cellular composition under variable environmental conditions may either mitigate or amplify ocean deoxygenation, particularly over longer timescales. Furthermore, we show that estimations of C^{soft} are sensitive to $R_{-\Sigma O2:C}$ and can lead to 213 Pg C difference (Table 3). Such a difference can induce a substantial bias when estimating the contribution of the biological pump to the total DIC inventory. Overall, our findings demonstrate that cellular-level biochemical reorganization under varying environmental conditions shape large-scale patterns of dissolved O_2 and C concentration.

MATERIALS AND METHODS

Estimating oxygen demand from bulk elemental composition

To estimate oxygen demand ($R_{-\Sigma O2:P}$) from bulk elemental composition ($C_aH_bO_cN_dP$), we followed the approach of Paulmier *et al.* (*12*). Organic matter is traditionally represented by the following formula: $(CH_2O)_x(NH_3)_yH_3PO_4$. To account for deviations from this idealized formula, particularly the excess hydrogen content, the formula can be rewritten as $C_x(H_2O)_wH_z(NH_3)_yH_3PO_4$. The oxygen required to oxidize both the reduced carbon (x) and the excess hydrogen (z) can be calculated as follows

$$C_x(H_2O)_wH_z(NH_3)_yH_3PO_4 + (x + 0.25z)O_2 \rightarrow xCO_2 + yNH_3 + H_3PO_4 + (w + 0.5z)H_2O$$

The elemental substitutions used are as follows: $x = a$, representing the number of carbon atoms, $w = c - 4$, assuming all oxygen not bound in H_3PO_4 is present as water (H_2O), $y = d$, representing the number of nitrogen atoms (assumed to be in the form of NH_3), $z =$

Downloaded from https://www.science.org at University of Rhode Island on November 06, 2026

$b - 2w - 3d - 3 = b - 2c - 3d + 5$, where the excess of hydrogen is calculated as the total hydrogen pool (b) minus the hydrogen in water ($2w$), ammonia ($3d$), and polyphosphate (3).

Ammonia oxidation proceeds through the following reactions

$$NH_3 + 3/2O_2 \rightarrow HNO_2 + H_2O$$

$$HNO_2 + 1/2O_2 \rightarrow HNO_3$$

$$NH_3 + 2O_2 \rightarrow HNO_3 + H_2O$$

Thus, ammonia oxidation consumes $2y$ moles of O_2.

The $R_{-\Sigma O2:P}$ for full oxidation of organic matter is given by

$$R_{-\Sigma O2:P} = x + 0.25z + 2y = a + 0.25\,(b - 2c - 3d + 5) + 2d$$

which simplifies to

$$R_{-\Sigma O2:P} = a + 0.25b - 0.5c + 1.25d + 1.25$$

The $R_{-\Sigma O2:C}$ for full oxidation of organic matter is given by

$$R_{-\Sigma O2:C} = (a + 0.25b - 0.5c + 1.25d + 1.25)/a$$

Here, a is the amount of oxygen required to oxidize carbon (as CH_2O), $2d$ accounts for oxygen required to oxidized reduced nitrogen, $0.25b - 0.5c - 0.75d + 1.25$ accounts for the oxygen required to oxidize excess hydrogen.

The macromolecular model

We simulated the macromolecular composition using the Cell Flux Model [CFM-phyto; (*27*, *34*)], which is now part of the Darwin model (*31*), the ecological and biogeochemical module embedded in the MIT general circulation model (*33*). Below, we outline several key model assumptions. Additional details are provided in the Supplementary Materials, and tables S1 and S4 to S8 list all symbol definitions and parameter values.

The CFM-phyto relies on the following assumptions:

1) Cellular carbon is constant

The carbon content of a phytoplankton cell, C_{Cell} [mol C (cell)$^{-1}$], increases due to photosynthesis and decreases due to cell division and maintenance. The rate of change is

$$\left(\frac{1}{C_{Cell}}\right)\frac{dC_{Cell}}{dt} = Q_C^{Chl} \cdot V_I - (1+E)\cdot\mu - m \quad (7)$$

where Q_C^{Chl} is the chlorophyll-to-carbon ratio [mol C in Chl (mol C)$^{-1}$], V_I is the chlorophyll-specific photosynthesis rate [mol C (mol C in Chl · day)$^{-1}$], μ is the growth rate (day^{-1}), E is the respiratory cost of biosynthesis (unitless), and m is the maintenance respiration rate (day^{-1}), which represents the amount of carbon required to maintain the cell and is not available for growth.

The photosynthesis rate V_I [mol C (mol C in Chl · day)$^{-1}$] is a saturating function of light I (μmol photons m^{-2} s^{-1})

$$V_I = V_I^{max} \cdot \left(1 - \exp^{-A_I \cdot I}\right) \quad (8)$$

Here, V_I^{max} [mol C (mol C in Chl · day)$^{-1}$] is the maximum chlorophyll-specific photosynthetic rate, and A_I is the light absorption cross-section and turnover time of the photosynthesis unit (m^2 s μmol^{-1}).

Assuming steady state $\left(\frac{dC_{Cell}}{dt} = 0\right)$, the chlorophyll-to-carbon ratio is

$$Q_C^{Chl} = \frac{(1+E)}{V_I}\cdot\mu + \frac{m}{V_I} \quad (9)$$

2) The composition of the photosynthetic apparatus is fixed and proportional to Q_C^{Chl}

$$Q_C^{Pro-Pho} = A_{Pho} \cdot Q_C^{Chl} \quad (10)$$

$$Q_P^{Thy} = A_{Pho}^{P} \cdot Q_C^{Chl} \quad (11)$$

$$Q_{Fe}^{Pho} = A_{Pho}^{Fe} \cdot Q_C^{Chl} \quad (12)$$

Here, $Q_C^{Pro-Pho}$ is C allocated to photosynthetic proteins [mol C (mol C)$^{-1}$], Q_P^{Thy} is P associated with phospholipids in thylakoid membranes [mol P (mol C)$^{-1}$], and Q_{Fe}^{Pho} is Fe in photosystems [mol Fe (mol C)$^{-1}$]. A_{Pho} [mol C (mol C in Chl)$^{-1}$], A_{Pho}^{P} [mol P (mol C in Chl)$^{-1}$], and A_{Pho}^{Fe} [mol Fe (mol C in Chl)$^{-1}$] are stoichiometric parameters (see table S1).

3) Allocation to biosynthetic protein and RNA scale linearly with growth rate

$$Q_C^{Pro-Bio} = A_{Bio} \cdot \mu \quad (13)$$

$$Q_P^{RNA} = A_{RNA}^{P} \cdot \mu \cdot \left(Q_C^{Pro-Bio} + Q_C^{Pro-Pho} + Q_C^{Pro-Other}\right) + Q_{P,min}^{RNA} \quad (14)$$

Here, $Q_C^{Pro-Bio}$ is carbon allocated to biosynthetic proteins [mol C (mol C)$^{-1}$], A_{Bio} is a proportionality constant [mol C (mol C)$^{-1}$ day], Q_P^{RNA} is P allocated to RNA [mol P (mol C)$^{-1}$], A_{RNA}^{P} is the proportionality constant for RNA investment [mol P (mol C)$^{-1}$ day], $Q_{P,min}^{RNA}$ is the minimum RNA quota at zero growth [mol P (mol C)$^{-1}$], and $Q_C^{Pro-Other}$ is a fixed pool of structural/essential proteins [mol C (mol C)$^{-1}$].

4) Preservation of cellular mass balance

Total cellular carbon (Q^C) is accounted for by the sum of all macromolecular pools (for symbols and units, see table S4)

$$Q^C = Q_C^{Pro-Pho}\ Q_C^{Pro-Bio} + Q_C^{Pro-Other} + Q_C^{RNA} + Q_C^{DNA} + Q_C^{Chl} + Q_C^{PLip} + Q_C^{Stor} + Q^{NStor}\cdot Y_{Nsto}^{C:N} + Q_C^{Other} \quad (15)$$

Here, $Q_C^{Pro-Pho}$, $Q_C^{Pro-Bio}$, and $Q_C^{Pro-Other}$ are cellular allocation to photosynthetic, biosynthetic, and "other" constant pool of structural proteins, respectively; Q_C^{RNA} and Q_C^{DNA} are carbon allocated to RNA and DNA; Q_C^{Chl} is the chlorophyll-to-carbon ratio; Q_C^{PLip} is carbon allocated to phospholipids; Q_C^{Stor} is carbon storage as carbohydrates and lipids; Q^{NStor} is carbon allocated to N storage; Q_C^{Other} is a pool of fixed carbon representing a nonflexible pool of structural lipids and carbohydrates; and $Y_{Nsto}^{C:N}$ is the C:N ratio in N storage.

Cellular N (Q^N) is accounted for by the sum of proteins ($Q_C^{Pro}\cdot Y_{Pro}^{N:C}$), where $Y_{Pro}^{N:C}$ is the N:C ratio in proteins, RNA (Q_N^{RNA}), DNA (Q_N^{DNA}), chlorophyll (Q_N^{Chl}), and N storage (Q^{NStor})

$$Q^N = Q_C^{Pro}\cdot Y_{Pro}^{N:C} + Q_N^{RNA} + Q_N^{DNA} + Q_N^{Chl} + Q^{NStor} \quad (16)$$

Cellular P (Q^P) is distributed among RNA (Q_P^{RNA}), DNA ($Q_C^{DNA} Y_{DNA}^{P:C}$), where $Y_{DNA}^{P:C}$ is the P:C ratio in DNA, phosphorus in

Downloaded from https://www.science.org at University of Rhode Island on November 06, 2026

thylakoid membrane (Q_P^{Thy}), phosphorus storage as polyphosphate (Q^{PStor}), and small fixed phosphorus pool (Q_P^{Other})

$$Q^P = Q_P^{RNA} + Q_C^{DNA} \cdot Y_{DNA}^{P:C} + Q_P^{Thy} + Q^{PStor} + Q_P^{Other} \quad (17)$$

Cellular iron (Q^{Fe}) is allocated to photosynthetic proteins (Q_{Fe}^{Pho}), and iron storage (Q^{FeStor})

$$Q^{Fe} = Q_{Fe}^{Pho} + Q^{FeStor} \quad (18)$$

Evaluating growth rate

We assume that carbon fixation rate (mmol C m^{-3} day^{-1}) for each phytoplankton j is given by

$$F_j = \mu_j \cdot c_j \quad (19)$$

where c_j is the biomass concentration of phytoplankton type j (mmol C m^{-3}) and μ_j is its specific growth rate (day^{-1}).

The growth rate μ_j is calculated by substituting the relationships above between cellular allocation and growth rate (Eqs. 9 to 14) in the cellular mass balances equations (Eqs. 15 to 18) and neglecting storage (Supplementary Materials).

The growth rate is constrained by the most limiting element

$$\mu_j = \min\left(\mu^C, \mu^N, \mu^P, \mu^{Fe}\right) \quad (20)$$

where μ^C, μ^N, μ^P, and μ^{Fe} are the carbon-, nitrogen-, phosphorus-, and iron-limited growth rates, respectively. These rates are derived from cellular mass-balance constraints and the macromolecular allocation model (Supplementary Materials).

The macromolecular pools are resolved in two phytoplankton, representing small prokaryotic-like phytoplankton (0.41 μm^3 cell volume) with high nutrient affinity and low growth rate and large eukaryote-like phytoplankton (40 μm^3 cell volume) with high growth rate and low nutrient affinity. Both phytoplankton are independently grazed by a single grazer. The two phytoplankton types differ in their maximum photosynthesis rates, maximum nutrient uptake rates, nutrient half-saturation constants, sinking rates, and palatability to grazers (tables S1 and S7).

Biogeochemical model

The equations governing phytoplankton and zooplankton carbon (c_j), phosphate (p_j), nitrogen (n_j), and iron (fe_j), all in mmol/m^3 are

$$\frac{Dc_j}{Dt} = F_j - M_j - G_j - S_j \quad (21)$$

$$\frac{Dp_j}{Dt} = U_j^P - M_j Q_j^P - G_j Q_j^P + g_j^P - S_j^P \quad (22)$$

$$\frac{Dn_j}{Dt} = U_j^N - M_j Q_j^N - G_j Q_j^N + g_j^N - S_j^N \quad (23)$$

$$\frac{Dfe_j}{Dt} = U_j^{Fe} - M_j Q_j^{Fe} - G_j Q_j^{Fe} + g_j^{Fe} - S_j^{Fe} \quad (24)$$

Here, D/Dt represents the material derivative that includes tracer transport; F represents phytoplankton net carbon fixation rates, which are calculated from the macromolecular model; U is nutrient uptake; M is the nongrazing mortality rate; G and g represent loss and gain from grazing, respectively; and S is sinking rates. Cellular quotas are defined as $Q_j^P = p_j / c_j$, $Q_j^N = n_j / c_j$, and $Q_j^{Fe} = fe_j / c_j$ (mol/mol C). $F = U = G = S = 0$ for zooplankton, and $g = 0$ for phytoplankton. Symbol definitions and units are in tables S5 and S6.

Dissolved nutrients

The concentrations of dissolved inorganic carbon, phosphorus, nitrogen, and iron (DIC, DIP, DIN, and DIFe, respectively) are governed by the following equations

$$\frac{DDIC}{Dt} = F_{CO2} + R_{DOC} + R_{POC} - \sum_j F_j \quad (25)$$

$$\frac{DDIP}{Dt} = R_{DOP} + R_{POP} - \sum_j F_j Q_j^P \quad (26)$$

$$\frac{DDIN}{Dt} = R_{DON} + R_{PON} - \sum_j F_j Q_j^N \quad (27)$$

$$\frac{DDIFe}{Dt} = R_{DOFe} + R_{POFe} - \sum_j F_j Q_j^{Fe} + S_{Fe} \quad (28)$$

where F_{CO2} is the air-sea gas exchange, R is respiration rates, F_j is the net carbon fixation rates, and S_{Fe} is external iron sources (table S6). PIC and alkalinity are not included in the model as the focus of this study is on the soft-tissue biological pump and its associated C and O_2 fluxes.

Particulate and dissolved organic matter

The model equations governing the formation, remineralization, and sinking of particulate (POi) and dissolved (DOi) organic matter (where i = C, H, N, O, P, and Fe) are

$$\frac{DPOi}{Dt} = f_j^{mort,POC} \sum_j M_j Q_j^i + g_j^{POi} - R_{POi} - S_{POi} \quad (29)$$

$$\frac{DDOi}{Dt} = \left(1 - f_j^{mort,POC}\right) \sum_j M_j Q_j^i + g_j^{DOi} - R_{DOi} \quad (30)$$

Here, $f_j^{mort,POC}$ is the fraction of phytoplankton and zooplankton mortality that goes the particulate pool, g is gain from grazing, R is respiration rate, and S is sinking rate. Cellular quotas Q_j^N, Q_j^P, and Q_j^{Fe} are computed from Eqs. 21 to 24. Q_j^H and Q_j^O are estimated from the macromolecular model (see section below).

Cellular oxygen and hydrogen

Cellular pools of organic hydrogen (Q_j^H) and oxygen (Q_j^O) are estimated from the macromolecular model

$$Q_j^H = Q_j^{C,Pro} Y_{Pro}^{H:C} + Q_j^{C,Carb} Y_{Carb}^{H:C} + Q_j^{C,Lip} Y_{Lip}^{H:C} + Q_j^{C,RNA} Y_{RNA}^{H:C} + Q_j^{C,DNA} Y_{DNA}^{H:C} + Q_j^{C,Chl} Y_{Chl}^{H:C} + Q_j^{C,Nsto} Y_{Nsto}^{H:C} \quad (31)$$

$$Q_j^O = Q_j^{C,Pro} Y_{Pro}^{O:C} + Q_j^{C,Carb} Y_{Carb}^{O:C} + Q_j^{C,Lip} Y_{Lip}^{O:C} + Q_j^{C,RNA} Y_{RNA}^{O:C} + Q_j^{C,DNA} Y_{DNA}^{O:C} + Q_j^{C,Chl} Y_{Chl}^{O:C} + Q_j^{C,Nsto} Y_{Nsto}^{O:C} \quad (32)$$

Downloaded from https://www.science.org at University of Rhode Island on November 06, 2026

Here, $Q_j^{C,Pro}$, $Q_j^{C,Carb}$, $Q_j^{C,Lip}$, $Q_j^{C,RNA}$, $Q_j^{C,DNA}$, $Q_j^{C,Chl}$, and $Q_j^{C,Nsto}$ are cellular allocation to proteins, carbohydrates, lipids, RNA, DNA, chlorophyll, and N-storage molecules (mol C/mol C), respectively, calculated from the macromolecular model (Supplementary Materials). $Y_j^{H:C}$ and $Y_j^{O:C}$ are the ratios of H:C and O:C in the different macromolecules (Fig. 1B).

The oxygen cycle

The model equation governing the dissolved oxygen concentration is

$$\frac{DO_2}{Dt} = F_{O2} + \sum_j RQ_j F_j - RQ_{DOC} R_{DOC} - RQ_{POC} R_{POC} \quad (33)$$

Here, F_{O2} is the air-sea gas-exchange flux (mmol O_2 m^{-3} day^{-1}), which depends on gas solubility, wind speed, and temperature (*73*), F_j is net carbon fixation rate (mmol C m^{-3} day^{-1}), R_{DOC} and R_{POC} are respiration rates (mmol C m^{-3} day^{-1}), and RQ_j (mmol O_2 mmol C^{-1}) is the respiration quotient of phytoplankton j

$$RQ_j = Q_j^{C,Pro} RQ_{Pro} + Q_j^{C,Carb} RQ_{Carb} + Q_j^{C,Lip} RQ_{Lip} + Q_j^{C,RNA} RQ_{RNA} + Q_j^{C,DNA} RQ_{DNA} + Q_j^{C,Chl} RQ_{Chl} + Q_j^{C,Nsto} RQ_{Nsto} \quad (34)$$

where RQ is the total respiration quotient of each macromolecule (Fig. 1B). The total respiration quotient of the dissolved- and particulate-organic matter (RQ_{POC} and RQ_{DOC}, respectively) is calculated by assuming a complete heterotrophic respiration of organic matter to CO_2 and NO_3 (Eq. 6 in Box 1)

$$RQ_{POC} = \frac{[POC] + 0.25[POH] + 1.25[PON] + 1.25[POP] - 0.5[POO]}{[POC]} \quad (35)$$

$$RQ_{DOC} = \frac{[DOC] + 0.25[DOH] + 1.25[DON] + 1.25[DOP] - 0.5[DOO]}{[DOC]} \quad (36)$$

Here, POC, POH, PON, POP, POO, DOC, DOH, DON, DOP, and DOO are the concentrations of dissolved and particulate organic carbon, hydrogen, nitrogen, phosphorus, and oxygen, respectively, calculated in Eqs. 29 and 30.

Physical model

The biogeochemical tracers are mixed and transported by the oceanic component of the MIT Integrated Global System Model (IGSM) (*74*–*76*). The IGSM is an Earth system model of intermediate complexity, featuring a two-dimensional (2D; latitude and height) atmosphere and a 3D ocean circulation model [the MITgcm; (*33*)] and is coupled to dynamic sea-ice and terrestrial models. The ocean component is configured here with a longitudinal resolution of 2.5° and a latitudinal resolution of 2°, and it has 22 nonuniform vertical depth levels, ranging from 10 m at the surface to 750 m at the bottom. We simulated the marine biogeochemical tracers for 2000 years using "offline" circulation fields from the ocean component of the IGSM for preindustrial (1860) conditions. After this spin-up, the biogeochemical tracers reach a quasi-steady state and are in reasonable agreement with global observations (figs. S6 and S7). An exception is the modeled surface phosphate concentration in the low-latitude Pacific, which is higher than observations (fig. S6, E and F). Nevertheless, the higher phosphate concentration is not expected to influence N:P, C:P, $R_{-\Sigma O2:P}$, and H:P ratios as phytoplankton in our model already take up polyphosphate until saturation as they are mostly limited by light, nitrate, and iron.

Dissolved O_2 concentrations along transects indicate that the model accurately captures the large-scale structure of interior O_2 distribution, showing good agreement in the Indian and Atlantic basins (fig. S9, A to D). In the Pacific, the model reproduces the presence of the oxygen minimum zones; however, it underestimates the deep-water O_2 levels (fig. S9, C and D). This underestimation of deep Pacific O_2 concentrations is likely associated with low vertical mixing as the mixing coefficients used do not allow oxygen to be transported into the deep waters to achieve the observed concentrations (*77*). The readers are referred to the citations above for further information.

Sensitivity of the global O_2 budget to the total respiration quotient ($R_{-\Sigma O2:C}$)

We conducted sensitivity experiments to diagnose the impact of total respiration quotient on the oceanic oxygen budget and the extent of the ocean hypoxic zones. In each of these simulations, the biogeochemical tracers were spun up for 2000 years with the offline physical circulation fields described above, where all the parameters were kept constant, except the total respiration quotient, which were set to the following values: (1) spatially variable $R_{-\Sigma O2:C}$, (2) spatially constant $R_{-\Sigma O2:C} = 1.3$, and (3) spatially constant $R_{-\Sigma O2:C} = 1.5$.

Case 1 is the spatially variable $R_{-\Sigma O2:C}$ found by our dynamic model (Fig. 4B). This experiment serves as the baseline for comparison with the other experiments. In case 2, we assume that the cells are mainly composed of carbohydrates. In this case $R_{-\Sigma O2:C}$ is spatially constant and equal to 1.3, representing subtropical phytoplankton. In case 3, we assume a spatially homogeneous $R_{-\Sigma O2:C}$ of 1.5. This scenario represents a situation where cells alter their composition to be predominantly composed of reduced proteins (i.e., high-latitude phytoplankton).

To calculate the global ocean inventory and the extent of the ocean hypoxic volumes (where dissolved O_2 concentrations are below 62 and 25 μM), we analyzed the model output after 2000 years of each simulation using MATLAB (Table 2).

After 2000 years, there remains a minor drift in the ocean O_2 inventory (~0.01 mmol O_2/m^3 per decade in mean concentration; fig. S6A), presumably due to a small number of extremely long-lived modes of the global ocean circulation (*78*, *79*). However, because the drift occurs in the same direction and at a similar rate across all simulations and because we compare each simulation relative to the default (first) experiment with variable total respiration quotient, we consider the impact of this drift on our results to be negligible.

Sensitivity of C^{soft} to the total respiration quotient

To diagnose the impact of spatially variable $R_{-\Sigma O2:C}$ on estimates of regenerated carbon from organic matter respiration (i.e., C^{soft}; Pg C), we used estimates of annual AOU diagnosed from observations of dissolved O_2, temperature, and salinity (*54*). AOU was regridded to the model resolution (144 × 90 × 23) using linear interpolation and converted to regenerated carbon by dividing it by the spatially variable $R_{-\Sigma O2:C}$ obtained by our study (Fig. 4D).

We compared these C^{soft} estimates with those calculated using spatially uniform $R_{-\Sigma O2:C}$ value of 1.3, 1.4, and 1.5. The value of 1.3 corresponds to the classical RKR value, assuming that a cell is composed fully of carbohydrates, 1.4 is the average ratio found in this study, and 1.5 is frequently used in global estimates of regenerated

Downloaded from https://www.science.org at University of Rhode Island on November 06, 2026

carbon (*51*, *52*). The regridded AOU, resulting C^{soft} distributions, and spatial differences among the estimates are shown in Fig. 7 and summarized in Table 3.

Supplementary Materials

This PDF file includes:

Supplementary Materials and Methods
Figs. S1 to S11
Tables S1 to S8
References

REFERENCES

1. D. Tilman, *Resource Competition and Community Structure* (Princeton Univ. Press, 1982).
2. M. J. Perry, R. W. Eppley, Phosphate uptake by phytoplankton in the central North Pacific Ocean. *Deep Sea Res. A Oceanogr. Res. Pap.* **28**, 39–49 (1981).
3. T. M. Lenton, A. J. Watson, Redfield revisited: 1. Regulation of nitrate, phosphate, and oxygen in the ocean. *Glob. Biogeochem. Cycles* **14**, 225–248 (2000).
4. M. M. Mills, K. R. Arrigo, Magnitude of oceanic nitrogen fixation influenced by the nutrient uptake ratio of phytoplankton. *Nat. Geosci.* **3**, 412–416 (2010).
5. C. Deutsch, T. Weber, Nutrient ratios as a tracer and driver of ocean biogeochemistry. *Annu. Rev. Mar. Sci.* **4**, 113–141 (2012).
6. B. A. Ward, S. Dutkiewicz, C. M. Moore, M. J. Follows, Iron, phosphorus, and nitrogen supply ratios define the biogeography of nitrogen fixation. *Limnol. Oceanogr.* **58**, 2059–2075 (2013).
7. W.-L. Wang, J. K. Moore, A. C. Martiny, F. W. Primeau, Convergent estimates of marine nitrogen fixation. *Nature* **566**, 205–211 (2019).
8. T. Volk, M. I. Hoffert, "Ocean carbon pumps: Analysis of relative strengths and efficiencies in ocean-driven atmospheric CO_2 changes," in *Geophysical Monograph Series*, E. T. Sundquist, W. S. Broecker, Eds. (American Geophysical Union, 1985), pp. 99–110.
9. W. S. Broecker, Ocean chemistry during glacial time. *Geochim. Cosmochim. Acta* **46**, 1689–1705 (1982).
10. E. D. Galbraith, A. C. Martiny, A simple nutrient-dependence mechanism for predicting the stoichiometry of marine ecosystems. *Proc. Natl. Acad. Sci. U.S.A.* **112**, 8199–8204 (2015).
11. L. A. Anderson, J. L. Sarmiento, Redfield ratios of remineralization determined by nutrient data analysis. *Glob. Biogeochem. Cycles* **8**, 65–80 (1994).
12. A. Paulmier, I. Kriest, A. Oschlies, Stoichiometries of remineralisation and denitrification in global biogeochemical ocean models. *Biogeosciences* **6**, 923–935 (2009).
13. A. R. Babbin, R. G. Keil, A. H. Devol, B. B. Ward, Organic matter stoichiometry, flux, and oxygen control nitrogen loss in the ocean. *Science* **344**, 406–408 (2014).
14. A. C. Redfield, *On the Proportions of Organic Derivatives in Sea Water and Their Relation to the Composition of Plankton* (University Press of Liverpool, 1934), vol. 1.
15. H. U. Sverdrup, W. J. Martin, H. F. Richard, *The Oceans: Their Physics, Chemistry, and General Biology* (Prentice-Hall, 1942), vol. 1087.
16. A. C. Redfield, B. H. Ketchum, F. A. Richards, "The influence of organisms on the composition of seawater," in *The Sea* (Interscience Publishers, ed. 2, 1963), pp. 26–77.
17. I. Morris, Photosynthetic products, physiological state, and phytoplankton growth. *Can. Bull. Fish. Aquat. Sci.* **210**, 83–102 (1981).
18. E. A. Laws, Photosynthetic quotients, new production and net community production in the open ocean. *Deep Sea Res. A Oceanogr. Res. Pap.* **38**, 143–167 (1991).
19. L. A. Anderson, On the hydrogen and oxygen content of marine phytoplankton. *Deep Sea Res. I Oceanogr. Res. Pap.* **42**, 1675–1680 (1995).
20. B. R. Carter, L. D. Talley, A. G. Dickson, Mixing and remineralization in waters detrained from the surface into Subantarctic Mode Water and Antarctic Intermediate Water in the southeastern Pacific. *J. Geophys. Res. Oceans* **119**, 4001–4028 (2014).
21. Y. Li, T. Peng, Latitudinal change of remineralization ratios in the oceans and its implication for nutrient cycles. *Glob. Biogeochem. Cycles* **16**, 77-1–77-16 (2002).
22. W. S. Broecker, T. Takahashi, T. Takahashi, Sources and flow patterns of deep-ocean waters as deduced from potential temperature, salinity, and initial phosphate concentration. *J. Geophys. Res. Oceans* **90**, 6925–6939 (1985).
23. T. Takahashi, W. S. Broecker, S. Langer, Redfield ratio based on chemical data from isopycnal surfaces. *J. Geophys. Res. Oceans* **90**, 6907–6924 (1985).
24. T. DeVries, C. Deutsch, Large-scale variations in the stoichiometry of marine organic matter respiration. *Nat. Geosci.* **7**, 890–894 (2014).
25. A. C. Martiny, C. T. A. Pham, F. W. Primeau, J. A. Vrugt, J. K. Moore, S. A. Levin, M. W. Lomas, Strong latitudinal patterns in the elemental ratios of marine plankton and organic matter. *Nat. Geosci.* **6**, 279–283 (2013).
26. S. Sharoni, I. Halevy, Nutrient ratios in marine particulate organic matter are predicted by the population structure of well-adapted phytoplankton. *Sci. Adv.* **6**, eaaw9371 (2020).
27. K. Inomura, C. Deutsch, O. Jahn, S. Dutkiewicz, M. J. Follows, Global patterns in marine organic matter stoichiometry driven by phytoplankton ecophysiology. *Nat. Geosci.* **15**, 1034–1040 (2022).
28. S. Sharoni, I. Keisuke, S. Dutkiewicz, O. Jahn, Z. Finkel, A. Irwin, E. Monier, M. J. Follows, Biochemical remodeling of phytoplankton cell composition under climate change. *Nat. Clim. Chang.* **16**, 494–500 (2026).
29. D. M. Karl, E. Grabowski, The importance of H in particulate organic matter stoichiometry, export and energy flow. *Front. Microbiol.* **8**, 826 (2017).
30. J. A. Raven, Predictions of Mn and Fe use efficiencies of phototrophic growth as a function of light availability for growth and of C assimilation pathway. *New Phytol.* **116**, 1–18 (1990).
31. M. J. Follows, S. Dutkiewicz, S. Grant, S. W. Chisholm, Emergent biogeography of microbial communities in a model ocean. *Science* **315**, 1843–1846 (2007).
32. S. Dutkiewicz, M. J. Follows, J. G. Bragg, Modeling the coupling of ocean ecology and biogeochemistry. *Glob. Biogeochem. Cycles* **23**, 2008GB003405 (2009).
33. J. Marshall, A. Adcroft, C. Hill, L. Perelman, C. Heisey, A finite-volume, incompressible Navier Stokes model for studies of the ocean on parallel computers. *J. Geophys. Res. Oceans* **102**, 5753–5766 (1997).
34. K. Inomura, A. W. Omta, D. Talmy, J. Bragg, C. Deutsch, M. J. Follows, A mechanistic model of macromolecular allocation, elemental stoichiometry, and growth rate in phytoplankton. *Front. Microbiol.* **11**, 86 (2020).
35. C. A. Klausmeier, E. Litchman, T. Daufresne, S. A. Levin, Optimal nitrogen-to-phosphorus stoichiometry of phytoplankton. *Nature* **429**, 171–174 (2004).
36. M. R. Sullivan, F. W. Primeau, G. I. Hagstrom, W. Wang, A. C. Martiny, Integrating trait-based stoichiometry in a biogeochemical inverse model reveals links between Phytoplankton physiology and global carbon export. *Glob. Biogeochem. Cycles* **38**, e2023GB007986 (2024).
37. C. M. Moore, M. M. Mills, K. R. Arrigo, I. Berman-Frank, L. Bopp, P. W. Boyd, E. D. Galbraith, R. J. Geider, C. Guieu, S. L. Jaccard, T. D. Jickells, J. La Roche, T. M. Lenton, N. M. Mahowald, E. Marañón, I. Marinov, J. K. Moore, T. Nakatsuka, A. Oschlies, M. A. Saito, T. F. Thingstad, A. Tsuda, O. Ulloa, Processes and patterns of oceanic nutrient limitation. *Nat. Geosci* **6**, 701–710 (2013).
38. G. I. Hagstrom, C. A. Stock, J. Y. Luo, S. A. Levin, Impact of dynamic phytoplankton stoichiometry on global scale patterns of nutrient limitation, nitrogen fixation, and carbon export. *Glob. Biogeochem. Cycles* **38**, e2023GB007991 (2024).
39. S. Roy, Distributions of phytoplankton carbohydrate, protein and lipid in the world oceans from satellite ocean colour. *ISME J.* **12**, 1457–1472 (2018).
40. J. D. Liefer, A. E. White, Z. V. Finkel, A. J. Irwin, M. Dugenne, K. Inomura, F. Ribalet, E. V. Armbrust, D. M. Karl, M. H. Fyfe, C. M. Brown, M. J. Follows, Latitudinal patterns in ocean C:N:P reflect phytoplankton acclimation and macromolecular composition. *Proc. Natl. Acad. Sci. U.S.A.* **121**, e2404460121 (2024).
41. N. Handa, K. Yanagi, K. Matsunaga, Distribution of detrital materials in the Western Pacific Ocean and their biochemical nature. *Mem. Natl. Inst. Polar Res* **53–71**, (1973).
42. S. D. Gerace, A. J. Fagan, F. W. Primeau, A. Moreno, P. J. Lethaby, R. J. Johnson, A. C. Martiny, Depth variance in the stoichiometry of marine organic matter and the implications for the global oxygen cycle. ESS Open Archive [Preprint] (2023). https://doi.org/10.22541/essoar.168295447.74227826/v1.
43. A. R. Moreno, C. A. Garcia, A. A. Larkin, J. A. Lee, W.-L. Wang, J. K. Moore, F. W. Primeau, A. C. Martiny, Latitudinal gradient in the respiration quotient and the implications for ocean oxygen availability. *Proc. Natl. Acad. Sci. U.S.A.* **117**, 22866–22872 (2020).
44. A. R. Moreno, A. A. Larkin, J. A. Lee, S. D. Gerace, G. A. Tarran, A. C. Martiny, Regulation of the respiration quotient across ocean basins. *AGU Adv.* **3**, e2022AV000679 (2022).
45. F. Fraga, A. F. Ríos, F. F. Pérez, F. G. Figueiras, Theoretical limits of oxygen:carbon and oxygen:nitrogen ratios during photosynthesis and mineralisation of organic matter in the sea. *Sci. Mar.* **62**, 161–168 (1998).
46. L. Stramma, G. C. Johnson, J. Sprintall, V. Mohrholz, Expanding oxygen-minimum zones in the tropical oceans. *Science* **320**, 655–658 (2008).
47. L. Bopp, L. Resplandy, J. C. Orr, S. C. Doney, J. P. Dunne, M. Gehlen, P. Halloran, C. Heinze, T. Ilyina, R. Séférian, J. Tjiputra, M. Vichi, Multiple stressors of ocean ecosystems in the 21st century: Projections with CMIP5 models. *Biogeosciences* **10**, 6225–6245 (2013).
48. L. Resplandy, Will ocean zones with low oxygen levels expand or shrink? *Nature* **557**, 314–315 (2018).
49. L. Kwiatkowski, et al., Twenty-first century ocean warming, acidification, deoxygenation, and upper-ocean nutrient and primary production decline from CMIP6 model projections. *Biogeosciences* **17**, 3439–3470 (2020). https://doi.org/10.5194/bg-17-3439-2020.
50. C. Robinson, Microbial respiration, the engine of ocean deoxygenation. *Front. Mar. Sci.* **5**, 533 (2019).
51. R. G. Williams, M. J. Follows, *Ocean Dynamics and the Carbon Cycle: Principles and Mechanisms* (Cambridge Univ. Press, 2011).
52. J. L. Sarmiento, *Ocean Biogeochemical Dynamics* (Princeton Univ. Press, 2013).
53. I. Frenger, A. Landolfi, K. Kvale, C. J. Somes, A. Oschlies, W. Yao, W. Koeve, Misconceptions of the marine biological carbon pump in a changing climate: Thinking outside the "export" box. *Global Chang. Biol.* **30**, e17124 (2024).
54. H. Garcia, K. Weathers, C. Paver, I. Smolyar, T. Boyer, M. Locarnini, A. Mishonov, O. Baranova, D. Seidov, J. Reagan, "World Ocean Atlas 2018. Volume 3: Dissolved oxygen,

Downloaded from https://www.science.org at University of Rhode Island on November 06, 2026

apparent oxygen utilization, and dissolved oxygen saturation" (NOAA Atlas NESDIS 83, 2019).
55. T. Ito, M. J. Follows, E. A. Boyle, Is AOU a good measure of respiration in the oceans? *Geophys. Res. Lett.* **31**, 2004GL020900 (2004).
56. W. S. Broecker, T. Takahashi, T. Peng, Reconstruction of past atmospheric CO_2 contents from the chemistry of the contemporary ocean: An evaluation. *Tech. Rep. TRO 20*, (1985).
57. M. Nowicki, T. DeVries, D. A. Siegel, Quantifying the carbon export and sequestration pathways of the ocean's biological carbon pump. *Glob. Biogeochem. Cycles* **36**, e2021GB007083 (2022).
58. L. Kwiatkowski, O. Aumont, L. Bopp, P. Ciais, The impact of variable phytoplankton stoichiometry on projections of primary production, food quality, and carbon uptake in the global ocean. *Glob. Biogeochem. Cycles* **32**, 516–528 (2018).
59. C.-T. Chien, M. Pahlow, M. Schartau, N. Li, A. Oschlies, Effects of phytoplankton physiology on global ocean biogeochemistry and climate. *Sci. Adv.* **9**, eadg1725 (2023).
60. G. Armin, K. Inomura, Modeled temperature dependencies of macromolecular allocation and elemental stoichiometry in phytoplankton. *Comput. Struct. Biotechnol. J.* **19**, 5421–5427 (2021).
61. F. P. Healey, Interacting effects of light and nutrient limitation on the growth rate of *Synechococcus linearis* (Cyanophyceae). *J. Phycol.* **21**, 134–146 (1985).
62. J. D. Liefer, A. Garg, M. H. Fyfe, A. J. Irwin, I. Benner, C. M. Brown, M. J. Follows, A. W. Omta, Z. V. Finkel, The macromolecular basis of phytoplankton C:N:P under nitrogen starvation. *Front. Microbiol.* **10**, 763 (2019).
63. S. T. Dyhrman, C. R. Benitez-Nelson, E. D. Orchard, S. T. Haley, P. J. Pellechia, A microbial source of phosphonates in oligotrophic marine systems. *Nat. Geosci.* **2**, 696–699 (2009).
64. F. M. Monteiro, S. Dutkiewicz, M. J. Follows, Biogeographical controls on the marine nitrogen fixers. *Glob. Biogeochem. Cycles* **25**, 10.1029/2010GB003902 (2011).
65. Z. V. Finkel, J. Beardall, K. J. Flynn, A. Quigg, T. A. V. Rees, J. A. Raven, Phytoplankton in a changing world: Cell size and elemental stoichiometry. *J. Plankton Res.* **32**, 119–137 (2010).
66. O. Einsle, D. C. Rees, Structural enzymology of nitrogenase enzymes. *Chem. Rev.* **120**, 4969–5004 (2020).
67. N. Handa, E. Tanoue, Organic compounds of the suspended particles in the Pacific sector of the Southern Ocean. *Mem. Natl. Inst. Polar Res Spec. Issue* **50–63**, (1983).
68. K. W. Becker, J. R. Collins, B. P. Durham, R. D. Groussman, A. E. White, H. F. Fredricks, J. E. Ossolinski, D. J. Repeta, P. Carini, E. V. Armbrust, B. A. S. Van Mooy, Daily changes in phytoplankton lipidomes reveal mechanisms of energy storage in the open ocean. *Nat. Commun.* **9**, 5179 (2018).
69. H. C. Holm, H. F. Fredricks, S. M. Bent, D. P. Lowenstein, J. E. Ossolinski, K. W. Becker, W. M. Johnson, K. Schrage, B. A. S. Van Mooy, Global ocean lipidomes show a universal relationship between temperature and lipid unsaturation. *Science* **376**, 1487–1491 (2022).
70. B. A. S. Van Mooy, H. F. Fredricks, B. E. Pedler, S. T. Dyhrman, D. M. Karl, M. Koblížek, M. W. Lomas, T. J. Mincer, L. R. Moore, T. Moutin, M. S. Rappé, E. A. Webb, Phytoplankton in the ocean use non-phosphorus lipids in response to phosphorus scarcity. *Nature* **458**, 69–72 (2009).
71. A. Oschlies, K. G. Schulz, U. Riebesell, A. Schmittner, Simulated 21st century's increase in oceanic suboxia by CO_2-enhanced biotic carbon export. *Glob. Biogeochem. Cycles* **22**, 2007GB003147 (2008).
72. L. Bopp, O. Aumont, L. Kwiatkowski, C. Clerc, L. Dupont, C. Ethé, T. Gorgues, R. Séférian, A. Tagliabue, Diazotrophy as a key driver of the response of marine net primary productivity to climate change. *Biogeosciences* **19**, 4267–4285 (2022).
73. R. Wanninkhof, Relationship between wind speed and gas exchange over the ocean. *J. Geophys. Res.* **97**, 7373–7382 (1992).
74. S. Dutkiewicz, A. Sokolov, J. Scott, P. H. Stone, "A three-dimensional ocean-seaice-carbon cycle model and its coupling to a two-dimensional atmospheric model: Uses in climate change studies" (MIT Joint Program of the Science and Policy of Global Change, 2005).
75. E. Monier, S. Paltsev, A. Sokolov, Y.-H. H. Chen, X. Gao, Q. Ejaz, E. Couzo, C. A. Schlosser, S. Dutkiewicz, C. Fant, J. Scott, D. Kicklighter, J. Morris, H. Jacoby, R. Prinn, M. Haigh, Toward a consistent modeling framework to assess multi-sectoral climate impacts. *Nat. Commun.* **9**, 660 (2018).
76. A. Sokolov, D. Kicklighter, A. Schlosser, C. Wang, E. Monier, B. Brown-Steiner, R. Prinn, C. Forest, X. Gao, A. Libardoni, S. Eastham, Description and evaluation of the MIT earth system model (MESM). *J. Adv. Model Earth Syst.* **10**, 1759–1789 (2018).
77. T. Ito, Y. Takano, C. Deutsch, M. C. Long, Sensitivity of global ocean deoxygenation to vertical and isopycnal mixing in an ocean biogeochemistry model. *Glob. Biogeochem. Cycles* **36**, e2021GB007151 (2022).
78. M. Holzer, F. W. Primeau, The diffusive ocean conveyor. *Geophys. Res. Lett.* **33**, 2006GL026232 (2006).
79. S. Khatiwala, F. Primeau, M. Holzer, Ventilation of the deep ocean constrained with tracer observations and implications for radiocarbon estimates of ideal mean age. *Earth Planet. Sci. Lett.* **325–326**, 116–125 (2012).
80. B. A. S. Van Mooy, H. F. Fredricks, Bacterial and eukaryotic intact polar lipids in the eastern subtropical South Pacific: Water-column distribution, planktonic sources, and fatty acid composition. *Geochim. Cosmochim. Acta* **74**, 6499–6516 (2010).
81. A. R. Fay, G. A. McKinley, Global open-ocean biomes: Mean and temporal variability. *Earth Syst. Sci. Data* **6**, 273–284 (2014).
82. T. Tanioka, A. A. Larkin, A. R. Moreno, M. L. Brock, A. J. Fagan, C. A. Garcia, N. S. Garcia, S. D. Gerace, J. A. Lee, M. W. Lomas, A. C. Martiny, Global ocean particulate organic phosphorus, carbon, oxygen for respiration, and nitrogen (GO-POPCORN). *Sci. Data* **9**, 688 (2022).
83. M. R. Brown, The amino-acid and sugar composition of 16 species of microalgae used in mariculture. *J. Exp. Mar. Biol. Ecol.* **145**, 79–99 (1991).
84. C. Lee, S. G. Wakeham, J. I. Hedges, Composition and flux of particulate amino acids and chloropigments in equatorial Pacific seawater and sediments. *Deep Sea Res. I Oceanogr. Res. Pap.* **47**, 1535–1568 (2000).
85. C. C. Sheridan, C. Lee, S. G. Wakeham, J. K. B. Bishop, Suspended particle organic composition and cycling in surface and midwaters of the equatorial Pacific Ocean. *Deep Sea Res. I Oceanogr. Res. Pap.* **49**, 1983–2008 (2002).
86. R. J. Siezen, T. H. Mague, Amino acids in suspended particulate matter from oceanic and coastal waters of the Pacific. *Mar. Chem.* **6**, 215–231 (1978).
87. MODIS, Global level 3 mapped SST, version 1, PO.DAAC (2022); https://modis.gsfc.nasa.gov/data/dataprod/chlor_a.php.
88. C. B. Mouw, A. Barnett, G. A. McKinley, L. Gloege, D. Pilcher, Global ocean particulate organic carbon flux merged with satellite parameters. *Earth Syst. Sci. Data* **8**, 531–541 (2016).
89. D. A. Hansell, C. A. Carlson, R. M. W. Amon, X. A. Álvarez-Salgado, Y. Yamashita, C. Romera-Castillo, M. B. Bif, "Compilation of dissolved organic matter (DOM) data obtained from global ocean observations from 1994 to 2021, version 2 (NCEI accession 0227166)" (NOAA National Centers for Environmental Information, 2021); www.ncei.noaa.gov/archive/accession/0227166.
90. R. T. Letscher, J. K. Moore, Preferential remineralization of dissolved organic phosphorus and non-Redfield DOM dynamics in the global ocean: Impacts on marine productivity, nitrogen fixation, and carbon export. *Glob. Biogeochem. Cycles* **29**, 325–340 (2015).
91. M. Piepho, M. T. Arts, A. Wacker, Species-specific variation in fatty acid concentrations of four phytoplankton species: Does phosphorus supply influence the effect of light intensity or temperature? *J. Phycol.* **48**, 64–73 (2012).

Acknowledgments: S.S. would like to thank all members of the Darwin group for the fruitful discussions and comments. We thank the Interuniversity Institute for Marine Sciences in Eilat for hosting S.S. Figures 2 to 7 and the supplementary figures were generated using MATLAB R2023a (The MathWorks Inc., Natick, MA, USA) with the Mapping Toolbox version 5.5. **Funding:** This work was supported by the Simons Foundation CBIOMES program (grant 549931 to M.J.F. and S.D.). S.S. acknowledges support from the Simons Foundation (grant LS-FMME-00004212), the Yad Hanadiv, Rothschild F 886 Foundation, and Fulbright Israel postdoc fellowship. K.I. acknowledges support from the Simons Foundation (grants 544338 and LS-ECIAMEE-00001549). **Author contributions:** Conceptualization: S.S. Methodology: S.S., K.I., S.D., O.J., and M.J.F. Software: S.D., O.J., S.S., and K.I. Validation: S.S. Formal analysis: S.S. Investigation: S.S. Resources: S.S., S.D., and K.I. Data curation: S.S., S.D., O.J., and G.L.B. Writing—original draft: S.S. Writing—review and editing: M.J.F., K.I., S.D., O.J., G.L.B., and S.S. Visualization: S.S. Supervision: M.J.F. Project administration: M.J.F. and S.S. Funding acquisition: M.J.F., S.S., and K.I. **Competing interests:** The authors declare that they have no competing interests. **Data, code, and materials availability:** All data and code needed to evaluate and reproduce the results in the paper are present in the paper and/or the Supplementary Materials. The source code, model outputs, and MATLAB scripts used in this study are available via Zenodo (https://doi.org/10.5281/zenodo.20522983). This study did not generate new materials.

Submitted 20 February 2026
Accepted 21 September 2026
Published 30 October 2026
10.1126/sciadv.aeg6228

Downloaded from https://www.science.org at University of Rhode Island on November 06, 2026

ScienceAdvances

C:H:N:O:P stoichiometry and oxygen demand of marine organic matter are driven by phytoplankton ecophysiology

Shlomit Sharoni, Keisuke Inomura, Stephanie Dutkiewicz, Oliver Jahn, Gregory L. Britten, and Michael J. Follows

Sci. Adv. **12** (44), eaeg6228. DOI: 10.1126/sciadv.aeg6228

View the article online
https://www.science.org/doi/10.1126/sciadv.aeg6228
Permissions
https://www.science.org/help/reprints-and-permissions

Downloaded from https://www.science.org at University of Rhode Island on November 06, 2026

Use of this article is subject to the Terms of service

Science Advances (ISSN 2375-2548) is published by the American Association for the Advancement of Science. 1200 New York Avenue NW, Washington, DC 20005. The title *Science Advances* is a registered trademark of AAAS.

Copyright © 2026 The Authors, some rights reserved; exclusive licensee American Association for the Advancement of Science. No claim to original U.S. Government Works. Distributed under a Creative Commons Attribution NonCommercial License 4.0 (CC BY-NC).